

# Preface

This work has been developed during a six-month internship at the Department of Applied Physics of the Eindhoven University of Technology (The Netherlands), in the frame of a collaboration with the Department of Energy Technologies of the University of Udine, (Italy). The work has been conducted under the supervision of Prof. Alfredo Soldati (Uniud), Prof. Federico Toschi (TU/e), Dr. Ing. Cristian Marchioli (Uniud) and Dr. Ing. Valentina Lavezzo (TU/e).

The results of this study will be presented at the 8<sup>th</sup> *International Workshop on Direct and Large – Eddy Simulation*, July 7-9 2010, Eindhoven, The Netherlands, with title *On The Error Estimate In Sub – Grid Models For Particles In Turbulent Flows*.



# Contents

<b>Preface</b>	<b>i</b>
<b>Abstract</b>	<b>xi</b>
<b>Sommario</b>	<b>xiii</b>
<b>1 Introduction</b>	<b>1</b>
1.1 Particles-turbulence interaction . . . . .	1
1.2 Turbulence wall structure . . . . .	6
1.3 Particle dynamics . . . . .	9
1.4 Two-particle Dispersion and Scope of this Work . . . . .	13
1.4.1 Single-particle Dispersion . . . . .	13
1.4.2 Two-particle Dispersion . . . . .	13
<b>2 Physical Modelling and Numerical Methodology</b>	<b>17</b>
2.1 Equation for the fluid phase and flow solver . . . . .	17
2.2 Equations for the dispersed phase and Lagrangian particle tracking . . . . .	19
2.3 Simulation Parameters . . . . .	22
2.4 Initial pairs arrangement . . . . .	24
<b>3 Results and Discussion</b>	<b>29</b>
3.1 Single-particle Statistics . . . . .	29
3.1.1 PDF of Single-particle Position . . . . .	29
3.1.2 Parametric Model for Particles Dispersion . . . . .	34
3.2 Pair dispersion . . . . .	40
3.2.1 Statistics . . . . .	40
3.2.2 Discussion . . . . .	48
<b>4 Conclusions</b>	<b>59</b>



# List of Figures

- 1.1 Influence of particle relaxation time on particle trajectory. Small inertia particles follow precisely the flow; large inertia particles filter the space changes of velocity; intermediate inertia particles respond selectively to the flow structures. . . . . 2
- 1.2 Effect of inertia on particle preferential sampling of a periodic vortical two-dimensional flow field reported by Maxey [25]: distribution of aerosol particles falling under gravity. The non-dimensional parameters characterizing aerosol motion are Stokes settling velocity for still fluid  $W = \tau_p g = 0.5$  and inertia parameter  $St = 0.2$ . . . . . 2
- 1.3 Particle-laden turbulent gas flow in a channel: sketch of the computational domain and minimal schematics of near-wall turbulent coherent structures. Strong causal relationship links low-speed streaks to ejections generated by quasi-streamwise vortices, which also generate in-sweeps of high streamwise momentum fluid to the wall in the high velocity regions. . . . 4
- 1.4 Instantaneous distribution of particles characterized by  $\tau_p = 116.3$  at time  $t^+ = 2700$ . View of particle position in the  $yz$ -plane for  $700 < x^+ < 1000$  (a) and corresponding  $xy$ -plane average number density distribution as a function of the wall normal direction (b). . . . . 5
- 1.5 Snapshot footprint of the wall shear-stress with corresponding sweep and ejection events in the whole computational domain. At the wall, red indicates high shear-stress; blue indicates low shear-stress. Gold 3D regions are isosurfaces characterizing sweeps whereas blue 3D regions characterize ejections. Iso-surfaces are traced at  $u'w' = -3$  in dimensionless units. . . . 7

1.6	(a) Quasi-streamwise counter-rotating vortices together with ejections and sweeps. Quasi-streamwise vortices extend for about 200 – 300 wall units. Two isosurfaces of the same absolute value of $\Omega$ indicate clockwise rotating (red) and counter-clockwise rotating (pale blue) vortices. Sweeps and ejections are indicated by green and blue, respectively. (b) Two counterrotating quasi-streamwise vortices onto a single low-speed streak (red). Green isosurface of $\Omega$ indicates clockwise rotating vortex, blue isosurface of $\Omega$ indicates counterclockwise rotating vortex. Picture covers a streamwise window about 450 wall units long. . . . .	8
1.7	(a) Macroscopic effect of particle interaction with turbulence structures. Particle number density distribution calculated from one way coupling simulations for particle time scales equal to 0.2, 1, 5 and 25 against non dimensional distance $z^+$ from the wall (logarithmic scale). The concentration profile reach a maximum very close to the wall; the non uniform trend is most pronounced for larger particles. (b) Top view of particle distribution in the boundary layer. Note accumulation of particles in specific regions which correspond to the low-speed streaks.	10
1.8	Cross section of instantaneous particle distribution in the $y-z$ plane for $\Delta x^+ = 400$ . . . . .	11
1.9	Cross section of the flow field and front view of particles in the region of particle accumulation. . . . .	12
1.10	Some smoke ejected by two chimneys and released by a fire in the atmospheric boundary layer. . . . .	14
1.11	The mean pair separation $\langle d^2(t) \rangle$ (indicated as $\langle r^2(t) \rangle$ in the figure) in a homogenous isotropic turbulent flow at $Re_\lambda = 383$ . The plot refers to DNS coupled to LPT of 307200 particles pairs. The scaling $\sim t^3$ in the inertial subrange is evident. . . .	15
2.1	The Kolmogorov length-scale $\eta_K^+$ (a) and time-scale $\tau_K^+$ (b) as a function of the wall-normal coordinate $z^+$ in the channel flow at $Re_\tau = 150$ . . . . .	23
2.2	The streamwise fluid velocity profile in the turbulent channel flow at $Re_\tau = 150$ . . . . .	24

2.3 The particles pairs are initially placed on 7 planes parallel to the walls in the bottom half of the channel, oriented along the streamwise (set = 1), spanwise (set = 2) and wall normal (set = 3) directions. The velocity gradient (shear) is used as a measure of non-homogeneity along the wall normal direction. . . . . 26

2.4 The relative statistic error,  $\sigma_u/\langle d \rangle$  [%]. . . . . 27

3.1 Some snapshots of particles instantaneous distribution at several crossing times ( $t^+/\tau_{ct} = 1/4, 1, 3, 8$ ). Particles are released on a plane at  $z_0^+ = 150$  (center of the channel).  $St = 25$ . . . . . 30

3.2 Some snapshots of particles instantaneous distribution at several crossing times ( $t^+/\tau_{ct} = 1/4, 1, 3, 8$ ). Particles are released on a plane at  $z_0^+ = 2$  (near the wall).  $St = 25$ . . . . . 31

3.3 Single-particle position PDF at several crossing times for particles released on a plane at  $z_0^+ = 150$  (a),  $z_0^+ = 37$  (b) and  $z_0^+ = 2$  (c). . . . . 32

3.4 The PDFs for  $St = 5, 25$  and  $125$  at  $t^+/\tau_{ct} = 1/4$  (a) and  $4$  (b). Particles distribution is almost the same for the three different particle sizes, especially at large times (b). An optimum for the segregation rate at the walls is found for  $St = 25$ . Particles are originally placed at  $z_0^+ = 150$ . . . . . 33

3.5 The variance of the gaussian distribution is shown for  $1 < t^+/\tau_{ct} < 3$ . Particles are originally placed at  $z_0^+ = 150$ . . . . . 34

3.6 A simple model for the law of the variance is obtained by a linear interpolation of the trend of  $\sigma^2$  for  $1 < t^+/\tau_{ct} < 2.3$ . Particles are originally placed at  $z_0^+ = 150$  (gaussian distribution). . . . . 36

3.7 Data of  $T$  and  $k$  and relative time-dependent laws obtained by interpolation are displayed. Particles are released at  $z_0^+ = 2$  (exponential distribution). . . . . 37

3.8 The trend of  $1/T$  (values of  $T$  are obtained fitting the PDFs).  $1/T$  is the slope of PDF's tail in logarithmic scale and it's also proportional to the term  $\frac{\partial \phi}{\partial z}$  in Fick's first law. We expect that  $1/T$  goes to zero after an infinite time, which corresponds to an homogeneous particle distribution in the central region of the channel. . . . . 38

- 3.9 Comparison between the PDFs for  $St = 5, 25$  and  $125$ , at two different times. At  $t^+/\tau_{ct} = 1$  (a) the three trends are very similar, while at  $t^+/\tau_{ct} = 8$  (b) a different slope for different Stokes numbers is observed. Particles are originally placed at  $z_0^+ = 2$ . . . . . 39
- 3.11 The variance  $\sigma^2 = \sum_{i=1}^N (d_i - \langle d \rangle)^2 / N$  is used as error bar to quantify the deviation of separation of each pair from the mean value. . . . . 40
- 3.10 The evolution of the mean square pair distance  $\langle d^2(t) \rangle$  for particles pairs released at  $z_0^+ = 150$ , (center of the channel),  $z_0^+ = 37$  and  $z_0^+ = 2$  (close to the wall) oriented along the streamwise, spanwise and wall normal direction respectively (set = 1, 2 and 3). Stokes number = 25 (intermediate size). Slopes are plotted just as trendlines (no data fit) in the inertial range (located between the horizontal lines). . . . . 41
- 3.12 The evolution of the mean square pair distance  $\langle d^2(t) \rangle$  for particles pairs released at  $z_0^+ = 150$ , (center of the channel),  $z_0^+ = 37$  and  $z_0^+ = 2$  (close to the wall) oriented along the streamwise direction. Comparison between  $St = 5, 25$  and  $125$ . Slopes are plotted just as trendlines (no data fit) in the inertial range. . . . 43
- 3.15 The *total mean exit time*  $\langle T(d) \rangle$  for pairs released at  $z_0^+ = 150$  oriented along the streamwise, spanwise and wall normal direction respectively (set = 1, 2 and 3). Stokes number = 125;  $\rho = 1.5$ . Slopes are plotted just as trendlines (no data fit). . . . 44
- 3.13 The mean exit time  $\langle T_p(d) \rangle$  for pairs released at  $z_0^+ = 150$ , (center of the channel),  $z_0^+ = 37$  and  $z_0^+ = 2$  (close to the wall) oriented along the streamwise, spanwise and wall normal direction respectively (set = 1, 2 and 3). Stokes number = 25 (intermediate size);  $\rho = 1.5$ . . . . . 45
- 3.14 The *total mean exit time* for pairs released at  $z_0^+ = 150$ , (center of the channel),  $z_0^+ = 37$  and  $z_0^+ = 2$  (close to the wall) oriented along the streamwise, spanwise and wall normal direction respectively (set = 1, 2 and 3). Stokes number = 25 (intermediate size);  $\rho = 1.5$ . Slopes are plotted just as trendlines (no data fit). 46

3.16 The mean longitudinal exit velocity  $\langle u_{||}(d) \rangle$  as a function of the separation  $d$  for pairs released at  $z_0^+ = 150$ , (center of the channel),  $z_0^+ = 37$  and  $z_0^+ = 2$  (close to the wall) oriented along the streamwise, spanwise and wall normal direction respectively (set = 1, 2 and 3). Stokes number = 25 (intermediate size);  $\rho = 1.5$ . Slopes are plotted just as trendlines (no data fit). 47

3.17 The mean shear  $du_x^+/dz^+$  along the wall normal direction in the channel flow. . . . . 48

3.18 Comparison between the shear  $du_x^+/dz^+$  and the inverse of the Kolmogorov time-scale  $\tau_K^+$ . In the center of the channel the small turbulence fluctuations are predominant on the shear and vice versa at the walls. . . . . 50

3.19 The mean square pair distance  $\langle d^2 \rangle$  compared with its three components:  $\langle d_x^2 \rangle$ ,  $\langle d_y^2 \rangle$  and  $\langle d_z^2 \rangle$ . At small times ( $t^+/\tau_{ct} < 1$ ),  $\langle d_x^2 \rangle \approx \langle d_y^2 \rangle \approx \langle d_z^2 \rangle$ . (a) At larger times ( $2 < t^+/\tau_{ct} < 3$ ), corresponding to the inertial subrange,  $\langle d^2 \rangle \approx \langle d_x^2 \rangle \sim t^9$  and  $\langle d_z^2 \rangle \sim t^6$ . Statistics are calculated on the all pairs. Particles are released at  $z_0^+ = 150$  oriented along the streamwise direction. A similar behavior was found for other wall normal locations and initial orientations. (b) At larger times ( $t^+/\tau_{ct} > 4$ ),  $\langle d^2 \rangle \approx \langle d_x^2 \rangle \sim t^7$ . Statistics are calculated only on the pairs that remain confined in the center of the channel, in the slab  $145 < z^+ < 155$ . The fluctuating trends of the lines at the end of the graph is due to the small number of pairs still within the very thin slab at long times. Slopes are plotted just as trendlines (no data fit). . . . . 52

3.20 The exponent  $\alpha$  of the slope of  $\langle d^2 \rangle$  in the inertial subrange for particles initially placed at the centerline ( $z_0^+ = 150$ ) and for different slabs of statistics computation. The shear is superimposed for comparison purposes. . . . . 53

- 3.21 Comparison between present results and results of Celani *et al.* [7] (a) At small times, Celani *et al.* recover Richardson prediction, while the anisotropy induced by the shear is negligible. As the separation becomes larger compared to the characteristic length scale of the shear, the latter affects particles trajectories and  $\langle d^2 \rangle \approx \langle d_x^2 \rangle \gg \langle d_y^2 \rangle$ , where the subscript  $y$  refers to the component orthogonal to the shear (that we name  $z$ ). In this range of scales,  $\langle d_x^2 \rangle \sim t^9$  and  $\langle d_y^2 \rangle \sim t^7$ . (b) Similarly, we find  $\langle d^2 \rangle \approx \langle d_x^2 \rangle \sim t^9$  in the inertial subrange, even if for a smaller range of time. The wall normal component cannot reach the inertial subrange before being affected by the shear and it evolves as  $\langle d_z^2 \rangle \sim t^6$  at the end of the dissipation subrange. Slopes are plotted just as trendlines (no data fit). (c) No plateau is observed around the slope  $\sim t^3$  in the dissipation subrange. . . . . 56
- 3.22 Comparison between present results and results of Celani *et al.* [7]. In Celani *et al.* the quantity  $S_2(r, 0)$ , shown in panel (a), is proportional to the time for two particles, initially coinciding, to reach a separation  $r$ , which is exactly the *total meanexit time*, shown in panel (b). Slopes are plotted just as trendlines (no data fit). This statistic shows the *uncontaminated* behavior of the particles pairs at several inter-particle distances. The plateau of the slope at a value of  $2/9 \approx 0.22$  in the inertial subrange is well appreciated (c). . . . . 57

# Abstract

Particle transport, dispersion, and segregation in turbulent flows are highly nonuniform and intermittent phenomena which are recognized to depend on the local dynamics of turbulence structures. A sound understanding and a thorough characterization of the mechanisms controlling particle transfer and segregation are of fundamental significance for a number of technological and environmental applications (e.g. mixing, combustion, depulveration, spray dynamics, pollutant dispersion, cloud dynamics...), and require deep comprehension of the interactions between particle dynamics and turbulent transport and mixing. Since inertia is a low-pass filter, particles respond selectively to turbulence fluctuations so that the system fluid turbulence-inertial particles may give rise to peak phenomena such as long-term local particle accumulation or segregation. In the specific case of boundary layers, this leads to irreversible particle segregation at the wall.

In this work we analyze the dispersion of micrometer size inertial particles by examining the behavior of particle pairs injected in a non-homogeneous, anisotropic turbulent shear flow. The specific physical problem considered for the study is fully-developed gas-solid turbulent channel flow. Pseudo-spectral Direct Numerical Simulation is carried out to calculate the flow field at bulk Reynolds number  $Re \simeq 2250$  (corresponding to a friction Reynolds number  $Re_\tau = 150$ ) in a 4 cm - high channel. Lagrangian tracking is used to describe the motion of large swarms of particles with different inertia, quantified by the dimensionless particle response time, referred to as Stokes number,  $St$ . The particle-to-fluid density ratio is  $O(10^3)$ . Particles of size  $d_p \cong 45, 100$  and  $230 \mu m$  were considered, corresponding to  $St = 5, 25$  and  $125$  respectively.

The main object of this study is to analyze the influence of both mean shear and small-scale turbulent fluctuations on the dispersion of particles. In particular, we will present time-dependent Probability Density Functions (PDFs) of single-particle distributions inside the flow domain and we will propose a simple parametric model to predict particle spreading. We will also present

particle pair dispersion statistics. In particular we will show both fixed-time and fixed-scale statistics, the latter being used to highlight the presence of an *uncontaminated* inertial subrange not affected by different particle pair separation rate. We will analyze these statistics systematically in an effort to isolate large-scale shear-induced effects from small-scale turbulence-induced ones. Shear-induced effects are expected to predominate in the near-wall region, where large velocity gradients occur, whereas small-scale fluctuations are expected to predominate in the nearly-homogeneous central region of the channel.

# Sommario

Il trasporto, la dispersione e la segregazione di particelle in flussi turbolenti sono fenomeni fortemente disuniformi ed intermittenti che dipendono dalle dinamiche locali delle strutture di turbolenza. Una solida conoscenza e una caratterizzazione approfondita dei meccanismi di controllo di trasferimento e segregazione particellare sono di primaria importanza per molte applicazioni tecnologiche ed ambientali (come ad esempio il mescolamento, la combustione, la depolverazione, spray, dispersione di inquinanti, moti delle nuvole...), e richiedono una profonda comprensione delle interazioni tra i moti delle particelle e il rimescolamento turbolento del fluido. Siccome l'inerzia è un filtro passa-basso, le particelle rispondono selettivamente alle fluttuazioni turbolente cosicchè il sistema flusso turbolento - particelle inerziali possono dare luogo a fenomeni di picco come accumulazioni o segregazioni locali di particelle a lungo periodo. Nel caso specifico di strati limite, ciò porta a segregazioni irreversibili delle particelle a parete.

Nel presente lavoro analizziamo la dispersione di particelle inerziali micrometriche studiando il comportamento di coppie di particelle iniettate in un flusso turbolento non omogeneo ed anisotropo dotato di shear. Il problema fisico specifico considerato nello studio è quello di un flusso turbolento gas-solido completamente sviluppato in canale. Il campo di moto del fluido è calcolato per mezzo di simulazioni numeriche dirette (DNS) mediante un metodo pseudo-spettrale, in un canale alto 4 cm e a numero di Reynolds bulk pari a  $Re \simeq 2250$  (corrispondente ad un friction Reynolds pari a  $Re_\tau = 150$ ). Si usa un tracciamento Lagrangiano per descrivere il moto di numerosi sciami di particelle dotate di differente inerzia, quest'ultima quantificata dal tempo di risposta adimensionale, espresso in termini di numero di Stokes,  $St$ . Il rapporto di densità particella/fluido è dell'ordine di  $10^3$ . Si considerano particelle di dimensioni  $d_p = 45, 100$  e  $230 \mu m$ , corrispondenti rispettivamente a  $St = 5, 25$  e  $125$ .

L'obiettivo principale del presente studio è analizzare l'influenza dello

shear medio e delle fluttuazioni turbolente di piccola scala sulla dispersione delle particelle. In particolare, presenteremo a diversi istanti temporali alcune Probability Density Functions (PDFs) sulle distribuzioni delle singole particelle all'interno del dominio e proporremo un semplice modello parametrico che sia in grado di predire la diffusione particellare. Presenteremo inoltre le statistiche sulle dispersioni delle coppie. In particolare mostreremo sia statistiche a tempi fissati che a scale fissate. Queste ultime sono usate per evidenziare la presenza di un range inerziale *incontaminato*, ovvero non influenzato dal differente grado di separazione tra le coppie che separano più lentamente e quelle che separano più velocemente. Analizzeremo sistematicamente queste statistiche, con lo sforzo di isolare gli effetti di larga scala prodotti dallo shear da quelli di piccola scala generati dalla turbolenza. Ci si aspetta che i primi siano prevalenti vicino a parete, dove si riscontrano elevati gradienti di velocità, mentre i secondi dovrebbero prevalere nella regione quasi omogenea di centro canale.

# Chapter 1

## Introduction

### 1.1 Particles-turbulence interaction

Decades of extensive studies have clarified several issues concerning particle dynamics. It is well known how inertial particles are subject to the actions of the surrounding fluid and a number of papers have been produced which examine the relative values of the fluid forces acting on particles (see [36] for instance). However, if particle density is much larger than fluid density (as in many cases of interest: dispersed flyashes, droplets, and heavy sediments) the largest effects on particle motion are due to drag and inertia with only small quantitative corrections produced by all other fluid forces actions. Thus, if particle diameter is not negligibly small, inertia will influence strongly particle behavior. The trajectory of an inertial particle driven by the drag force in a vortical flow field is sketched in Fig.1.1 in which solid lines represent tracer pathlines. In Fig.1.1, the behavior of three different inertia particles is controlled by the particle time-scale – particle relaxation time – which, from the steady-state balance between inertia and the linear Stokes drag, is defined as  $\tau_p = \rho_p d_p^2 / 18\mu$ , where  $\rho_p$ ,  $d_p$ , and  $\mu$  are particle density, particle diameter, and fluid dynamic viscosity, respectively. In Fig.1.1, particles with different time-scale are subject to the same flow time-scale,  $\tau_f$ , defined on the basis of the inverse of vorticity. The ratio of the particle relaxation time to the flow time-scale defines the Stokes number as  $St = \tau_p / \tau_f$ . Broadly speaking, particles act as a low-pass filter responding to the flow scales larger than their time-scale. If their time-scale is comparable to the fluid time-scale, particles may be propelled into specific flow regions and tend to sample the flow field in a preferential way.

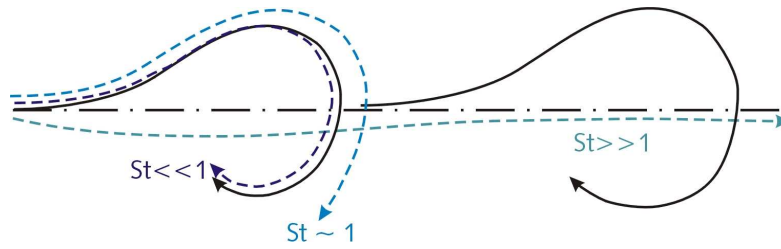


Figure 1.1: Influence of particle relaxation time on particle trajectory. Small inertia particles follow precisely the flow; large inertia particles filter the space changes of velocity; intermediate inertia particles respond selectively to the flow structures.

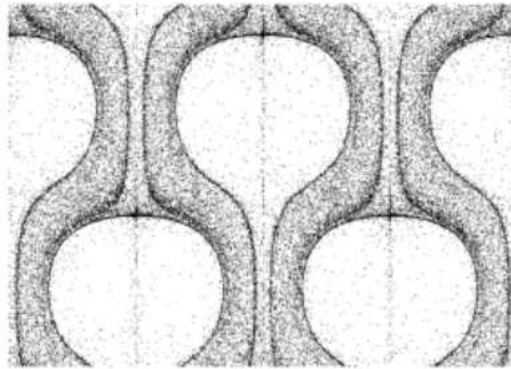


Figure 1.2: Effect of inertia on particle preferential sampling of a periodic vortical two-dimensional flow field reported by Maxey [25]: distribution of aerosol particles falling under gravity. The non-dimensional parameters characterizing aerosol motion are Stokes setting velocity for still fluid  $W = \tau_p g = 0.5$  and inertia parameter  $St = 0.2$ .

This concept was demonstrated by Maxey [25] examining the behavior of swarms of inertial particles in a two-dimensional, periodic field of simple cellular vortices. In his numerical experiment, particles were settling under gravity and showed a tendency to sample the flow field preferentially. The same experiment was reproduced by Soldati [36] and results of particle preferential distribution are shown in Fig.1.2: The effect is striking for this type of model steady flow and suggests that insights into real three-dimensional, time-dependent turbulent dispersions may be obtained by trying to identify the archetypal dynamics of the dominant flow structures.

Real three-dimensional time-dependent turbulent fields are characterized by vortical structures of largely different scales mutually interacting. Particles will be thus advected in a fashion which is not at all random and will assume a spatially intermittent distribution. This effect will be amplified or damped

depending on the particle-to-flow time-scale ratio [29, 10].

Preferential segregation of particles is fundamental in a number of turbulent flow applications [5, 30]. Yet, in the specific case of turbulent boundary layer, the local interaction between particles and turbulence structures leads to a remarkably unique macroscopic behavior, i.e. particle accumulation in the viscous sublayer [4, 18]. This macroscopic behavior is due to the combined action of the many microscopic transfer phenomena which drive particles toward the wall and away from the wall. Since 1957, when Friedlander and Johnstone [11] in the context of deposition theory broadly differentiated between the behavior of large and small particles in the viscous sublayer, much attention was dedicated to investigation of particle wall transfer mechanisms. In 1975, Cleaver and Yates [8] proposed a sub-layer model based on the Reynolds analogy for particle transport in turbulent boundary layer for the deposition of small solid particles from a gas stream. According to this mechanism, particles are driven toward the wall and away from the wall by sweeps – coherent downwash of outer fluid to the wall – and ejections – coherent upwash of wall fluid toward the outer flow – which are instantaneous realizations of the Reynolds stresses – Q4 and Q2 type events respectively [35].

Of course, since early times efforts, Reynolds averaging of the Navier-Stokes equations assigned a crucial role to Q2 and Q4 events, yet it is only after the paper by Kline et al. [21] that they have been dignified as coherent structures together with the other time and space persistent flow phenomena in the boundary layer. The remarkable papers by Hussain [13] simplified the understanding of turbulence phenomena pinpointing that a clear identification and a correct definition of coherent structures were the key to understand possible archetypal dynamics in turbulent flows. This theoretical tool assisted by the rapidly increasing computational power, which finally made feasible long-desired, three-dimensional, time-dependent, fully-resolved turbulent flow simulations, produced an entire branch of flourishing literature which gave new hopes in turbulence research by looking for coherent structures through the wealth of data available from Direct Numerical Simulation (DNS). In particular, many questions about the dynamics of turbulent boundary layers have been addressed and answered identifying the different characteristic coherent structures and proposing mechanisms to explain their generation process (the turbulence regeneration mechanism).

There is a general consensus on the dynamics of turbulence structures in the boundary layer and the coherent structures have been precisely classified. Henceforth, we refer to a flow inside a channel. The reference geometry con-

sists of two infinite flat parallel walls: the origin of the coordinate system is located at the center of the channel and the  $x$ -,  $y$ - and  $z$ -axes point in the streamwise, spanwise and wall-normal directions respectively (see Fig.1.3). The statistically most common coherent structures are single streamwise-oriented vortices, generally centred within the buffer layer. Quasi-streamwise vortices generate strongly coherent sweeps on the downwash side and strongly coherent ejections on the upwash side.

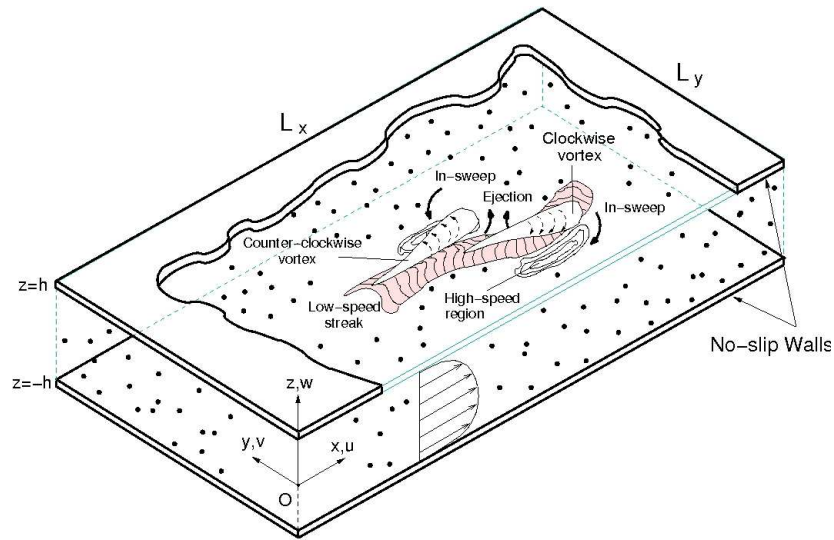


Figure 1.3: Particle-laden turbulent gas flow in a channel: sketch of the computational domain and minimal schematics of near-wall turbulent coherent structures. Strong causal relationship links low-speed streaks to ejections generated by quasi-streamwise vortices, which also generate in-sweeps of high streamwise momentum fluid to the wall in the high velocity regions.

In the outer region, several recent investigations suggest that the most common vortex structures appear like hairpins whose legs are the counter-rotating quasi-streamwise vortices populating the near-wall region. Neither these hairpins usually possess perfect spanwise symmetry nor the counter-rotating vortices have equal strength. Spanwise axisymmetric one-sided hairpins are also observed. These new models revise and improve the classical concept of  $\Omega$ -shaped horseshoe vortices and are widely, though not totally, accepted. In recent papers, Zhou et al. [37] and Adrian et al. [1] proposed a new mechanism for turbulence regeneration cycle which is based on packets of hairpin vortices travelling at the same convection velocity, a new fundamental super-structure. Apparently, these super-structures populate all regions of the turbulent boundary layer and their characteristics fit well with most of previous quantitative observations from Kline et al. [21] up to the most recent. Furthermore, Adrian

et al. [1] report that if we focus our attention only to the near wall region – i.e. less than 60 wall units from the wall – the phenomenology of the hair-pin packet is very similar to the structures proposed by Schoppa and Hussain [32, 13] and Jeong et al. [15].

Despite the great progress in the investigation of turbulence structures and dynamics, an equal effort was not produced in the area of turbulent dispersed flows. Several features of particle behavior in the boundary layer are broadly established, yet there are still many open issues concerning particle transfer mechanisms and particle segregation. In particular, even though the initial intuition by Cleaver and Yates [8] can be granted, quantitative evaluations are not yet broadly available. In addition, physical models which can explain why particles tend to accumulate at the wall, appear not completely explored. Still not fully understood are reasons and modalities under which, once at the wall, particles remain trapped in the low streamwise velocity regions at a distance from the wall not exceeding few wall units even when gravity does not play a role, both in horizontal flows with neutrally buoyant particles and in vertical flows.

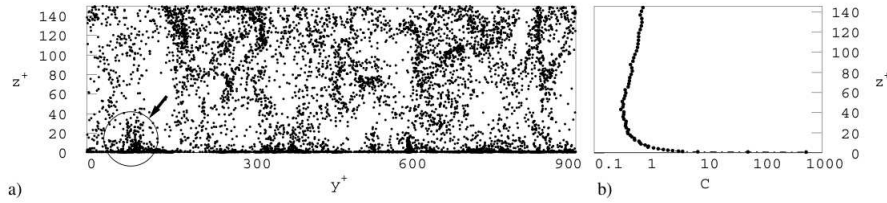


Figure 1.4: Instantaneous distribution of particles characterized by  $\tau_p = 116.3$  at time  $t^+ = 2700$ . View of particle position in the  $yz$ -plane for  $700 < x^+ < 1000$  (a) and corresponding  $xy$ -plane average number density distribution as a function of the wall normal direction (b).

Several of the above mentioned phenomena are shown in Fig.1.4(a) together with a number of features which can help us to focus on the process of particle dispersion and transfer in turbulent boundary layer. First, we observe that particles are not homogeneously distributed along the channel. In particular, particles tend to cluster around large vortical structures. From these clusters, particles are transported toward the wall, accumulating into specific “reservoirs” (one of these is indicated by the black circle) where concentration build-up occurs. These accumulation regions are characterized by flow streamwise velocity lower than the mean. Particles tend to stay long times in these low-speed regions so that eventually particle concentration increases

near the wall. To quantify near-wall accumulation, the particle number density distribution is plotted as a function of the non dimensional distance from the wall ( $z^+$ ) in Fig.1.4(b). A logarithmic scale is used for particle number concentration to capture the detail of particle behavior in the proximity of the wall. The concentration profile is developing with time, and at the instant shot in Fig.1.4(b), we observe that particle number density profile has developed a maximum well into the near-wall region ( $0 < z^+ < 20$ ). This behavior can be viewed as the consequence of the turbulence non-homogeneity, and has been observed in a number of previous works.

## 1.2 Turbulence wall structure

In a turbulent boundary layer, momentum, heat, and mass transfer are controlled by the instantaneous realizations of the Reynolds stresses. Ejections and sweeps – Q4 and Q2 type events, respectively – control momentum transfer at the wall and are also well correlated to heat transfer and mass transfer at the wall. Specifically, ejections bring the low-momentum fluid close to the wall into the outer region whereas sweeps bring the high-momentum fluid from the outer flow into the wall region. A complete characterization of sweeps and ejections and of their generation mechanisms is thus fundamental to understand the physics of turbulence structure at the wall and to explain the effect produced on particle dynamics. The snapshot shown in Fig.1.5 visualizes sweeps, ejections, and their action of momentum transfer to the wall. In this figure, flow is from left to right along the  $x$  direction. Sweeps (gold lumps) and ejections (blue lumps) are identified with the same value of the instantaneous stress isosurface at  $u'w' = -3$  in wall units. To visualize the correlations “sweep-high shear stress” and “ejection-low shear stress” the wall is colored with the intensity of the instantaneous shear stress at the wall – blue is low and red is high. It is apparent that low shear-stress regions correspond to the ejections, whereas high shear-stress regions correspond to the sweeps.

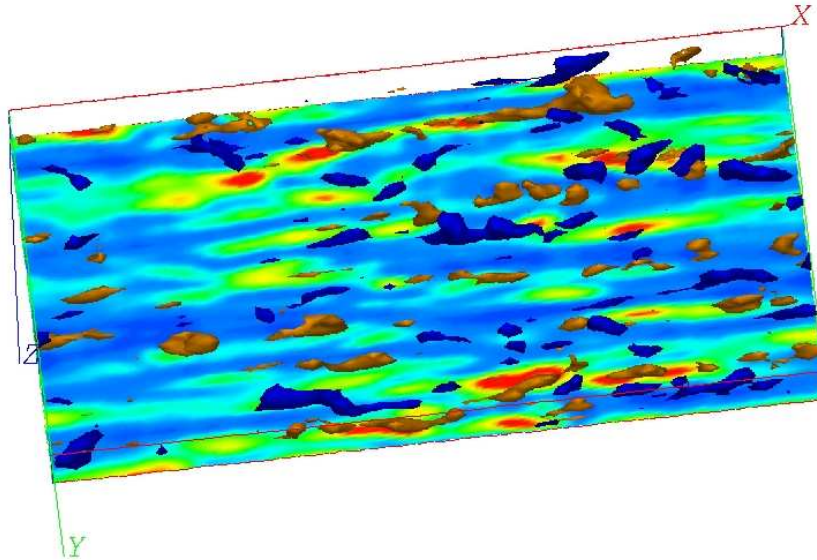


Figure 1.5: Snapshot footprint of the wall shear-stress with corresponding sweep and ejection events in the whole computational domain. At the wall, red indicates high shear-stress; blue indicates low shear-stress. Gold 3D regions are isosurfaces characterizing sweeps whereas blue 3D regions characterize ejections. Isosurfaces are traced at  $u'w' = -3$  in dimensionless units.

Sweeps and ejections are just a chain ring of wall turbulence regeneration cycle, and there is still some uncertainty about the mechanisms which generate and maintain the sweep/ejection events. They appear to be generated by the quasi-streamwise vortices which populate the near wall region. Quasi-streamwise vortices are slightly tilted away from the wall and are responsible for pumping fluid towards and away from the wall. Clockwise and counter-clockwise rotating vortices are slightly tilted upward - about 9 average [32]; and are also slightly tilted about 4 left and right, respectively. The stream-wise vortices may be identified by using pressure, vorticity, or other indicators [12]. A broadly-used method for identification exploits the streamline rotation vector  $\Omega$  to visualize vortices as flow regions where the rate-of-deformation tensor  $\partial u_i / \partial x_j$  exhibits complex eigenvalues [27]. From a physical viewpoint, the vector  $\Omega$  represents strength and direction of the rotation of the streamlines.

In Fig. 1.6(a), two counter-rotating vortices, identified by one isosurface of  $\Omega$ , are shown together with the ejections and sweeps they generate. The elongated red and pale blue structures are two isosurfaces with the same absolute value of  $\Omega$  (and opposite sign) and indicate clockwise rotating (red) and coun-

terclockwise rotating (pale blue) vortices. Flow is going from bottom left to top right and vortices appear tilted away from the wall by the mean strain rate. The blue lumps of fluid in between the two vortices are ejections and the green lumps of fluid outside the two vortices are sweeps. Ejections and sweeps also appear stretched streamwise and affected by the mean strain rate. Owing to the continuous action of the quasi-streamwise vortices in generating sweeps and ejections, regions between two vortices such as those shown in Fig.1.6 are characterized by a streamwise velocity lower than the mean low-speed streaks, whereas the regions outside the two vortices are characterized by a streamwise velocity higher than the mean high-speed regions.

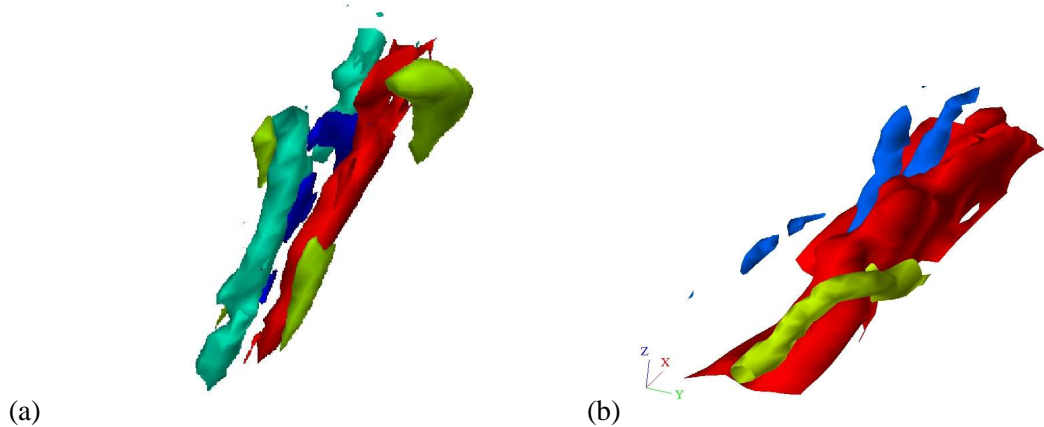


Figure 1.6: (a) Quasi-streamwise counter-rotating vortices together with ejections and sweeps. Quasi-streamwise vortices extend for about 200 – 300 wall units. Two isosurfaces of the same absolute value of  $\Omega$  indicate clockwise rotating (red) and counterclockwise rotating (pale blue) vortices. Sweeps and ejections are indicated by green and blue, respectively. (b) Two counterrotating quasi-streamwise vortices onto a single low-speed streak (red). Green isosurface of  $\Omega$  indicates clockwise rotating vortex, blue isosurface of  $\Omega$  indicates counterclockwise rotating vortex. Picture covers a streamwise window about 450 wall units long.

Many quasi-streamwise vortices are usually associated with one single low-speed streak. Low-speed streaks are sinuous regions about 1000 wall units long and are more coherent than high-speed regions.

In Fig.1.6(b), a 450 wall units long piece of one low-speed streak is shown, flanked by two counter-rotating quasi-streamwise vortices. The red isosurface identifies a streamwise velocity value of  $0.56U_c$ , where  $U_c$  is centerline velocity, which is broadly considered the advection velocity of the low-speed streak.

In this figure, the action of the quasi-streamwise vortices in lifting up the low-speed streak is clear. Streamwise vortical structures overlap streamwise as a staggered array, as was clearly demonstrated by Schoppa and Hussain [32, 13]. One single low-speed streak has a longer life than quasi-streamwise vortices and survives a number of vortex generations. It has been shown [20] that the generation of the quasi-streamwise vortices is associated with lateral instabilities producing changes in the shape of the low-speed streak surface. In recent papers, Schoppa and Hussain [32, 13] suggested that wall turbulence is dominated by a cycle in which low-speed streaks generate quasi-streamwise vortices, which in turn generate ejections and sweeps. These finally contribute to maintain the low-speed streaks.

Thus, the view of evolutionary dynamics of boundary layers structures changes perspective in that streaks are considered responsible for the initial generation of quasi-streamwise vortices. Based on this view, Schoppa and Hussain [32, 13] suggest different strategies for turbulence control. The most interesting strategy seems to be stabilization of the low-speed streaks by means of large-scale forcing motions. In practice, a low-speed streak which is more stable to spanwise perturbations would reduce its meandering and reduce the tripping frequency of quasi-streamwise vortices eventually reducing the frequency and the intensity of turbulence production events – i.e. sweeps and ejections.

### 1.3 Particle dynamics

There is experimental and numerical evidence that heavy particles in turbulent boundary layer have a tendency to migrate toward the wall under the turbophoretic drift [4, 6, 26]. Fig.1.7(a) shows the particle number density concentration plotted as a function of the non dimensional wall distance  $z^+$ . A logarithmic scale is used to capture the detail of particle distribution in the near-wall region. Particle number concentration is normalized to the initially uniform concentration and is calculated after 1125 time wall units. As discussed by Portela et al. [28], particle distribution is not yet statistically steady. Regardless of particle size, number concentration is non-uniform along the wall normal coordinate, the trend being most pronounced for larger particles. In particular, the concentration profile appears to reach a maximum very close to the wall. This behavior can be viewed as the consequence of non-uniform turbulence advection mechanisms, the intensity of which decreases to very low values in the near wall region.

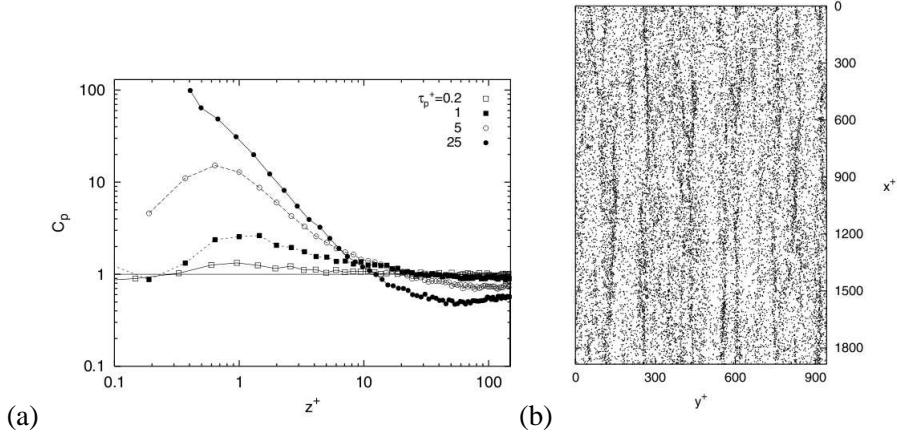


Figure 1.7: (a) Macroscopic effect of particle interaction with turbulence structures. Particle number density distribution calculated from one way coupling simulations for particle time scales equal to 0.2, 1, 5 and 25 against non dimensional distance  $z^+$  from the wall (logarithmic scale). The concentration profile reach a maximum very close to the wall; the non uniform trend is most pronounced for larger particles. (b) Top view of particle distribution in the boundary layer. Note accumulation of particles in specific regions which correspond to the low-speed streaks.

Number concentration is non-uniform also in the wall parallel direction, with particles segregated preferentially in regions characterized by streamwise velocity lower than the mean. Fig.1.7(b) shows the instantaneous distribution of  $\tau_p = 25$  particles in the region between the wall and  $z^+ = 3$ . The tendency of inertial particles to accumulate in the low-speed regions may support a possible use of particles as smart roughness. In real situations, characterized by flow field modulation by the particles, the presence of particles would increase the inertia of the low-speed streaks. Since low-speed streak stability to lateral perturbation has an impact on the wall turbulence regenerat cycle, the presence of specific inertia or size particles in turbulent boundary layer might be exploited to tune wall transfer mechanisms.

In Fig.1.8 we show an instantaneous cross section in the  $(y-z)$  plane of particle distribution. Specific regions of particle accumulation are clearly visible. These regions identify the main gateways for particle transfer to the wall region. In a previous work Marchioli and Soldati [23] examined the relationship between particle fluxes in and out the wall layer and momentum fluxes at the wall. They found that particles are transferred almost exclusively by strongly coherent sweeps and ejections: Specifically, a strong correlation exists between sweep events and particle flux toward the wall, and between ejection events and particle flux toward the outer flow. This correlation is almost

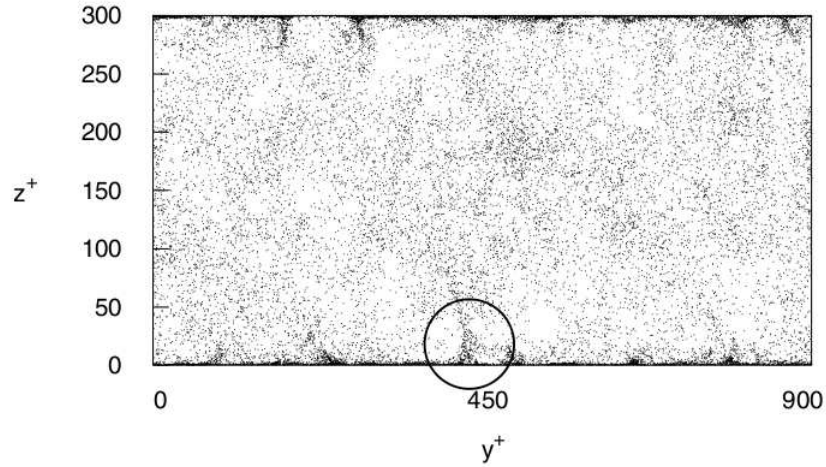


Figure 1.8: Cross section of instantaneous particle distribution in the  $y - z$  plane for  $\Delta x^+ = 400$ .

perfect for smaller particles and somehow weaker for larger particles. In other words, if a small particle travels toward the wall, it is entrained in a sweep whereas if the particle travels away from the wall, it is driven by an ejection. For larger particles, most of the particles are still transferred by sweeps and ejections but a higher proportion of particles with positive wall normal velocity appears in fluid environments characterized by negative wall-normal velocity, and viceversa. In particular, for the larger sets of particles, the fraction of particles travelling toward the wall in a non-sweep environment is smaller than the fraction of particles travelling away from the wall in a non-ejection environment [23].

This behavior is easily attributed to the *local* particle Stokes number which increases along the Lagrangian trajectory of the particle which, while travelling toward the wall, interacts with smaller and smaller flow structures. The characteristic time-scale of turbulent structures scales linearly with wall distance and decreases progressively as the structures lie closer to the wall. The strongly coherent sweeps which transfer effectively particles to the wall are generated by the forward-end of the mature quasi-streamwise vortical structures which is located in the buffer layer. Larger particles have a larger time-scale and filter out the effects of the smaller fluid scales. Thus, the larger momentum gained by the large particles in the strongly coherent sweep is able to drive them to the wall and may be sufficient to let the particle bounce elastically off the wall, crossing the smaller scale structures in the vicinity of the wall unable to further modify the trajectory of the particle.

Particle Stokes number is also responsible for particle accumulation under

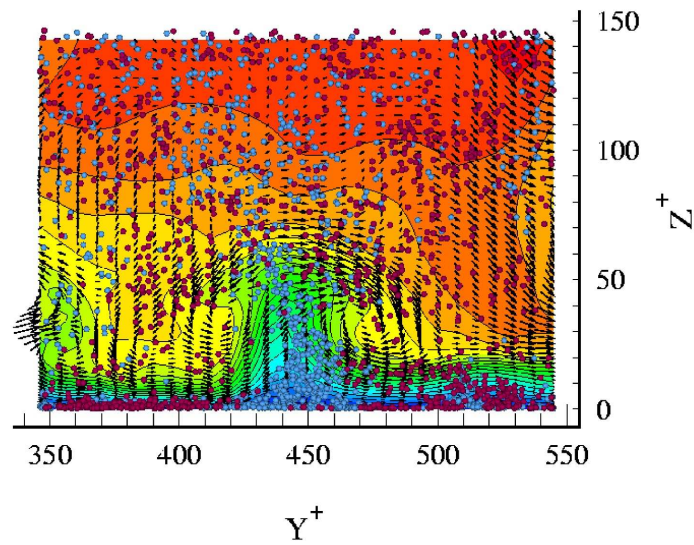


Figure 1.9: Cross section of the flow field and front view of particles in the region of particle accumulation.

the low-speed streaks. Fluid obeys continuity and fluid fluxes to the wall must be balanced by counterfluxes away from the wall. Particles, however, behave somehow as a compressible fluid and may accumulate as precisely according to what is happening to the small swarm of particles circled in Fig.1.8, which is undergoing a strongly coherent phenomenon. Fig.1.9 shows a cross section of the flow field in the region of particle accumulation. Vectors represent velocity components in the plane and color isocontours show the values of the streamwise velocity component. A strongly coherent ejection is present in the middle of the figure and indicates the position of the low-speed streak which appears lifted and flanked by two counter-rotating vortical structures. Particle position is identified with the circles – larger than the real scale for visualization purposes. Blue particles have wall normal velocity directed away from the wall ( $\omega_p > 0$ ) whereas purple particles have wall-normal velocity directed toward the wall ( $\omega_p < 0$ ). In the outer region, say above  $z^+ > 100$ , there is no evident correlation between particle wall-normal velocity and fluid streamwise velocity. Approaching the wall, however, virtually all particles entrained in the ejection – streamwise velocity lower than the mean – have positive wall normal velocity indicating an extremely focused and coherent event. Particles approaching the wall are entrained in the two sweep events – yellow regions. Depending on the momentum they acquire, particles directed towards the wall may reach it or may follow the flow streaklines approaching the ejection to be

re-entrained in the outer flow.

## 1.4 Two-particle Dispersion and Scope of this Work

### 1.4.1 Single-particle Dispersion

Arguably the most elemental understanding one can have of any flow field is how particles are moved by the flow. Conceptually, it is far simpler to consider the trajectory of a particle than it is to fully comprehend the velocity vector field. The motion of particles is also important because of its connection with the processes of transport and mixing that impact natural and engineering flows in such profound ways. Indeed, it is the latter application that drew the attention of some of the greatest minds in fluid mechanics to the study of particle motion in turbulence. The original work of Taylor (1922) on single-particle dispersion gave birth to many of the modern statistical tools we use to study turbulence. In particular, a literature survey reveals that many numerical and experimental studies have been performed to examine tracers dispersion from a line source orthogonal to wall normal direction [17, 19, 14]. The first purpose of this work is to present single particle statistics of inertial particles released at a certain distance from the walls. This study may have interesting industrial and environmental applications, such as pollution dispersion in the atmospheric boundary layer (see Fig.1.10). For instance, it can be useful to predict in first approximation where and when the smoke released from a chimney at a certain altitude will reach the ground, if it will stratify somewhere or well disperse in the sky. Indeed, in the center of the channel the shear influence is almost null and then its bottom-half ( $0 < z^+ < 150$ ) can well represent the atmospheric boundary layer.

### 1.4.2 Two-particle Dispersion

Richardson (1926) was the first that examined the relative motion of two particles embedded in isotropic turbulence, establishing the foundations of two-particle dispersion. There is a fundamental link between the formal analysis of pair dispersion and practical problems such as the growth relative to the center of mass of a cloud of contaminants in the atmosphere, nutrients in the ocean, or chemical species in a turbulent reactor. In all these examples that involve fluid flow, a nondimensional parameter that represents the ratio of inertial and viscous forces is the Reynolds number, here defined in terms of the Taylor microscale as  $Re_\lambda \equiv \langle u^2 \rangle^{1/2} \lambda / \nu$ , where  $\langle u^2 \rangle^{1/2}$  is the root mean square of the



Figure 1.10: Some smoke ejected by two chimneys and released by a fire in the atmospheric boundary layer.

fluctuating velocity,  $\nu$  is the fluid kinematic viscosity,  $\lambda \equiv \sqrt{15\nu \langle u^2 \rangle / \langle \varepsilon \rangle}$ , and  $\varepsilon$  is the turbulent energy dissipation rate. Laboratory and industrial flows are characterized by  $Re_\lambda O(10^2 - 10^3)$ , whereas geophysical flows can reach  $O(10^4)$  and higher.

If we consider two particles initially separated by the distance  $\mathbf{d}(t=0) = d_0 = \mathbf{d}_1(0) - \mathbf{d}_2(0)$  and placed in a turbulent flow field, we expect that their distance will change in time. The instantaneous separation of the position of the particles is  $\mathbf{d}(t) = \mathbf{d}_1(t) - \mathbf{d}_2(t)$ . We can divide the process of dispersion into three distinct regimes based on the separation of the particles relative to the turbulent scales: (a) The *dissipation subrange* corresponds to  $d(t) \ll \eta_K$ , where  $\eta_K \equiv (\nu^3 / \langle \varepsilon \rangle)^{1/4}$  is the Kolmogorov length-scale; (b) the *inertial subrange* corresponds to  $\eta_K \ll d(t) \ll L$ , where  $L$  is the integral length scale; and (c) the *diffusion subrange* corresponds to  $d(t) \gg L$ . The analysis and scaling for each subrange are unique and they are explained in detail by Salazar and Collins [29]. In this work we will focus on what happens in the inertial subrange.

As the particle pair separates beyond the dissipation scales, the range of

motions (or eddy sizes) that move them apart varies with the separation distance, in which eddies of scale  $l \sim d(t)$  are most effective in the process of dispersion (Corrsin 1962). Richardson (1926) initially put forth this notion and suggested a specific diffusion equation for relative dispersion in isotropic turbulence. Compiling measurements of the effective eddy diffusion coefficient and making other assumptions, he found a solution which implied that

$$\langle d^2(t) \rangle = g \langle \varepsilon \rangle t^3, \quad (1.1)$$

where  $g$  is called *Richardson's constant*. Many computational and laboratory experiments [2, 3, 16] confirmed this trend in the inertial subrange of two and three-dimensional isotropic turbulent flows. In Fig.1.11 an example of the scaling  $\langle d^2(t) \rangle \sim t^3$  obtained by a DNS is shown.

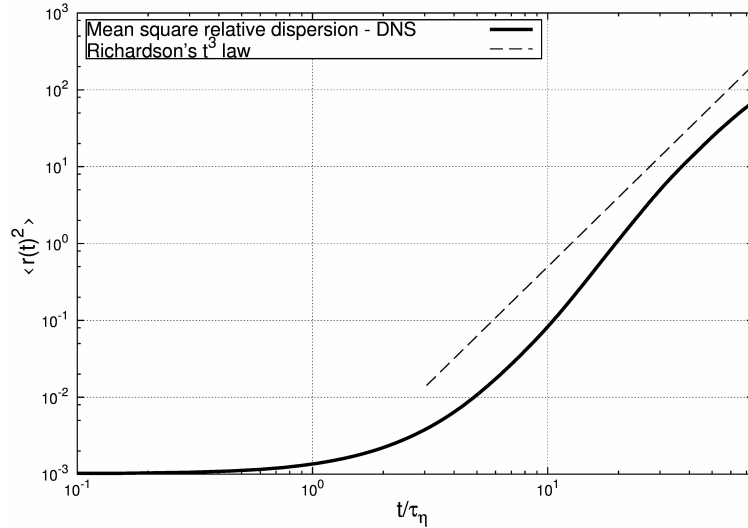


Figure 1.11: The mean pair separation  $\langle d^2(t) \rangle$  (indicated as  $\langle r^2(t) \rangle$  in the figure) in a homogenous isotropic turbulent flow at  $Re_\lambda = 383$ . The plot refers to DNS coupled to LPT of 307200 particles pairs. The scaling  $\sim t^3$  in the inertial subrange is evident.

Homogeneous isotropic turbulence is the simplest configuration for studying the statistics of relative dispersion, but it has limited application to real situations. An investigation in turbulent flows affected by the presence of solid boundaries should be dutiful. Another limitation introduced in most experiment is due to the use of tracers, i.e., massless particles. This latter are able to follow precisely the flow and then they provide the most accurate informations about fluid motions, even for the smallest scales. Furthermore, tracers are preferred to inertial particles in DNS because it is sufficient to integrate in time

the equation

$$\frac{d\mathbf{x}}{dt} = \mathbf{v} \quad (1.2)$$

to track all the history of particle motion,  $\mathbf{v}$  being the velocity of the fluid at particle position. This greatly reduce computational efforts. Despite these merits, tracers do not well simulate behavior of real particles, especially when these have a mass not negligible with respect to the physical of the problem.

The main scope of this work is to study the pair dispersion of inertial particles in a turbulent channel flow. Particularly, we want to get informations about the rate of scaling in the inertial subrange and the influence of the strong shear near the walls on two-particle statistics. To this aim, we track some swarms of particles released at different distances from the walls and measure statistics along the pair trajectories both as a function of time and as a function of their separation, i.e., at fixed scales. A comparison with homogeneous isotropic turbulence in the center of the channel is reasonable, the flow being few affected by the two walls in the region around the centerline. We also present some single particle statistics regarding swarm's distribution in the channel, to correlate wall segregation with pair dispersion.

## Chapter 2

# Physical Modelling and Numerical Methodology

To investigate the physics of particle pairs, we performed direct numerical simulations (DNS) of gas-solid channel flow. The reference geometry consists of two infinite flat parallel walls: the origin of the coordinate system is located at a corner of the channel and the  $x$ -,  $y$ - and  $z$ - axes point in the stream-wise, spanwise and wall-normal directions respectively (see Fig.1.3). Periodic boundary conditions are imposed on the fluid velocity field in the homogeneous directions ( $x$  and  $y$ ), no-slip boundary conditions are imposed at the walls ( $z = 0$  and  $z = 2h$ ). The size of the computational domain is  $L_x \times L_y \times L_z = 4\pi h \times 2\pi h \times 2h$ . In this work, we will consider non-reactive, isothermal and incompressible (low Mach number) flow and monodispersed micrometer-size particles: in particular, we will consider Newtonian fluid (specifically, air with density  $\rho = 1.3 \text{ kg m}^{-3}$  and kinematic viscosity  $\nu = 1.57 \times 10^{-5} \text{ m}^2 \text{ s}^{-1}$  and pointwise heavy particles (with density  $\rho_p = 1000 \text{ kg m}^{-3}$ ). Fluid and particle properties in dimensional form are given here for the sake of providing a possible application of our simulations to a *real* physical instance.

### 2.1 Equation for the fluid phase and flow solver

In our studies, we have performed DNS of fully-developed channel flow. In DNS, the governing balance equations for the fluid in dimensionless form read as (cit Soldati and Banerjee, 1998):

$$\frac{\partial u_i}{\partial x_i} = 0, \quad (2.1)$$

$$\frac{\partial u_i}{\partial t} = -u_j \frac{\partial u_i}{\partial x_j} + \frac{1}{Re} \frac{\partial^2 u_i}{\partial x_j^2} - \frac{\partial p}{\partial x_i} + \delta_{1,i}, \quad (2.2)$$

where  $u_i$  is the  $i^{th}$  component of the dimensionless velocity vector,  $p$  is the fluctuating kinematic pressure,  $\delta_{1,i}$  is the mean dimensionless pressure gradient that drives the flow whereas  $Re_\tau = u_\tau h/\nu$  is the shear Reynolds number based on the shear (or friction) velocity,  $u_\tau$ , and on the half channel height,  $h$ . The shear velocity is defined as  $u_\tau = \sqrt{\tau_w/\rho}$ , where  $\tau_w$  is the mean shear stress at the wall. All variables are taken in dimensionless form, represented by the superscript + (which has been dropped from Eqns.2.1 and 2.2 for ease of reading) and expressed in wall units. Wall units are obtained combining  $u_\tau$ ,  $\nu$  and  $\rho$ .

The flow solver used to perform the numerical simulations is based on a pseudo-spectral method that transforms the field variables into wave space to discretize the governing equations. In the homogeneous directions ( $x$  and  $y$ ), all the quantities are expressed by Fourier expansions using  $k_x$  and  $k_y$  wavenumbers. In the wall-normal non-homogeneous direction, they are represented by Chebyshev polynomials. The solution, represented spectrally in all three flow directions, have the general form:

$$\mathbf{u}(k_x, k_y, n) = \sum_{k_x} \sum_{k_y} \sum_n \hat{\mathbf{u}}(k_x, k_y, n) e^{i(k_x x + k_y y)} T_n(z), \quad (2.3)$$

in which  $T_n(z) = \cos[n \cdot \cos^{-1}(z/h)]$  is the  $n$ -th order Chebyshev polynomial. By using the orthogonality property of  $e^{i(k_x x + k_y y)}$ , the equations for the Fourier coefficients  $\hat{\mathbf{u}}(k_x, k_y, n)$  can be obtained. All the differential equations to be solved are of Helmholtz type with Neumann, Dirichlet or mixed boundary conditions specified at the walls. Time advancement of the equations is done by the two-level explicit Adams-Bashforth scheme for the non-linear convection terms and by the implicit Crank-Nicolson method for the diffusion terms. All the calculations are carried out in wave space except the evaluation of the nonlinear terms, which is done in physical space and then transformed back to wave space in order to avoid the convolution summations which reduce the efficiency of the method. This numerical scheme is quite standard for directly simulating turbulent flows in domains of simple geometry, such as rectangular channels (cit Soldati and Banerjee, 1998).

## 2.2 Equations for the dispersed phase and Lagrangian particle tracking

In the Lagrangian framework, the motion of particles is described by a set of ordinary differential equations for particle velocity and position. These equations in vector form read as:

$$\frac{d\mathbf{x}}{dt} = \mathbf{v}, \quad (2.4)$$

$$\begin{aligned} \frac{d\mathbf{v}}{dt} = & \left(1 - \frac{\rho_f}{\rho_p}\right) \mathbf{g} - \frac{3C_D}{4} \frac{C_D}{d_p} \left(\frac{\rho_f}{\rho_p}\right) |\mathbf{v} - \mathbf{u}| (\mathbf{v} - \mathbf{u}) + \\ & \frac{\rho_f}{\rho_p} \frac{D\mathbf{u}}{Dt} + C_L \frac{\rho_f}{\rho_p} [(\mathbf{u} - \mathbf{v}) \times \boldsymbol{\omega}] + \frac{\rho_f}{2\rho_p} \left(\frac{D\mathbf{u}}{Dt} - \frac{d\mathbf{v}}{dt}\right) + \\ & \frac{9\mu}{d_p \rho_p \sqrt{\pi v}} \int_0^t \left(\frac{d\mathbf{u}}{d\tau} - \frac{d\mathbf{v}}{d\tau}\right) \frac{d\tau}{(t - \tau)^{0.5}}, \end{aligned} \quad (2.5)$$

where  $\mathbf{x}$  and  $\mathbf{v}$  are the particle instantaneous position and velocity;  $\mathbf{u}$  and  $\boldsymbol{\omega}$  are the fluid velocity and vorticity at the particle position;  $d_p$  and  $\rho_p$  are the particle diameter and the particle material density;  $\mu$  is the fluid dynamic viscosity; and  $\mathbf{g}$  is gravitational acceleration. The time derivative  $d/dt$  is calculated following the moving particle ( $d\mathbf{u}/dt = \partial\mathbf{u}/\partial t + \mathbf{v} \cdot \nabla\mathbf{u}$ ), whereas  $D\mathbf{u}/Dt$  is the total acceleration of the fluid instantaneously evaluated at the particle position ( $D\mathbf{u}/Dt = \partial\mathbf{u}/\partial t + \mathbf{u} \cdot \nabla\mathbf{u}$ ). Each term in Eq. 2.5 represents forces per unit mass acting on a particle. The term on the left-hand side represents particle inertia, whereas the right-hand side terms describe the effect of gravity, Stokes drag ( $C_D$  being the drag coefficient), pressure gradient, aerodynamic lift ( $C_L$  being the lift coefficient), added mass and time-history Basset, respectively. This equation is similar to the equation of motion for small rigid spheres discussed by Maxey and Riley [24], in which the second-order terms have been neglected due to the small size of the particles. Here, the Stokes drag coefficient is computed using the following non-linear correction [31]:  $C_D = \frac{24}{Re_p} (1 + 0.15Re_p^{0.687})$  where  $Re_p = d_p |\mathbf{v} - \mathbf{u}| / \nu$  is the particle Reynolds number. The correction for  $C_D$  is necessary when  $Re_p$  does not remain small [9].

The evolution of particle position and velocity is obtained upon time-integration of the above equations. In the Lagrangian framework, a computational particle represents only one physical particle and, therefore, time integration is performed for each individual particle to be tracked. To minimize the computa-

tional effort required by this operation, which scales as the number of tracked particles  $n_p$ , eq.2.5 can be simplified in a suitable manner. Simplification is made based on the relative importance of each force in the considered flow configuration, which in turn depends on several particle parameters. Depending on the specific value of these relevant parameters, some terms in eq.2.5 can be neglected without loss of accuracy in the final result. For particles much heavier than the fluid ( $\rho_p/\rho_f \gg 1$ ), the most significant forces are Stokes drag and gravity. Other forces acting on the particle, such as Basset, fluid pressure gradient and added mass can be neglected being at least one order of magnitude smaller: The contributions of hydrostatic force, Magnus effect and Brownian diffusion can be neglected as well because of the specific set of physical parameters of our simulations. One last contribution to be considered carefully is that due to the lift force. Previous studies showed that, for small particles, the lift force term becomes formally of the same order in particle radius as other terms we neglected in the more complete equation of motion derived by Maxey and Riley [24]. In this situation, the lift force is small compared to the particle drag in the same direction and is expected to produce slight quantitative (yet not qualitative) modifications of the deposition statistics. For larger particles, however, the lift force may have significant effects on the rate of particle accumulation near the wall, particularly in presence of a solid boundary. The influence of the lift force in determining the buildup of particle concentration in the viscous sublayer is in turn modulated by gravity, which acts to increase/decrease the slip velocity between particles and fluid via the well-known crossing-trajectory effect [25].

For the purposes of performing a phenomenological study of turbulent particle pair dispersion, we start from a base simulation in which the setting is kept as simplified as possible. To minimize the number of degrees of freedom, we neglect the effect of gravity and lift in the first instance. A simplified version of the Basset-Boussinesq-Oseen equation is thus obtained. In vector form:

$$\frac{d\mathbf{v}}{dt} = \frac{(\mathbf{u} - \mathbf{v})}{\tau_p} (1 + 0.15Re_p^{0.687}), \quad (2.6)$$

where  $\tau_p = \rho_p d_p^2 / 18\mu$  is the particle relaxation time, a measure of particle inertia denoting the time scale with which any slip velocity between the particles and the fluid is equilibrated. Subsequent inclusion of additional forces (gravity and lift in our problem) can be done to single out their specific effect on particles and to analyze possible qualitative and quantitative changes to the

scenario depicted by the base simulation.

To calculate individual particle trajectories in the flow field, we have coupled a Lagrangian particle tracking (LPT) routine to the DNS flow solver. The routine solves for Eqns. 2.6 and 2.4 under the following assumptions: (i) particles are pointwise, non-rotating rigid spheres (point-particle approach); (ii) particles are injected into the flow at concentration low enough to consider dilute system conditions: the effect of particles onto the turbulent field is neglected (one-way coupling approach) as well as inter-particle collisions. These assumptions lead to a simplified physical model. This model, however, still provides the proper level of description to extract physical knowledge from a complex two-phase system and, therefore, it is fully representative of the main qualitative features of the phenomena investigated.

The equations of particle motion are advanced in time using a 4<sup>th</sup>-order Runge-Kutta scheme: at the beginning, particles are randomly distributed on planes orthogonal to wall normal direction, as described in Sec. 2.4, and their initial velocity is set equal to that of the fluid at the particle initial position. Periodic boundary conditions are imposed on particles moving outside the computational domain in the homogeneous directions. Perfectly-elastic collisions at the smooth walls are assumed when the particle center is at a distance lower than one particle radius from the wall (note that the data sets obtained assuming perfectly reflecting walls can be used to extract subsets of data for the case of perfectly absorbing walls simply by tagging time and location of the particle upon impact). The timestep size used for particle tracking was chosen to be equal to the timestep size used for the fluid,  $\delta t^+ = 0.045$ . This time step size is more than 20 times smaller than the non-dimensional response time of the smallest particle tracked (see Sec. 2.4 for details).

An accurate calculation of the forces acting on the particle requires careful evaluation of the instantaneous fluid velocity at the particle location. This is a critical issue in LPT and, therefore, many papers dealing with the interpolation problem are available in the archival literature. A wide variety of interpolation methods has been tested in channel flow. Both high-order hybrid schemes (see for instance Yeung and Pope [36], who tested both a third-order Taylor-series interpolation scheme and a cubic-spline scheme) and lower-order time-efficient schemes have been employed. Considering previous analyses, we decided to use an interpolation scheme based on 6<sup>th</sup>-order Lagrangian polynomials: near the wall, the interpolation scheme switches to one-sided. The performance of the interpolation scheme is comparable to that of spectral direct summation and to that of an hybrid scheme which exploits sixth-order

Lagrangian polynomials in the homogeneous directions and Chebyshev summation in the wall-normal direction. This second approach is highly accurate and the computational work requirement was smaller than the computational work requirement for a fully spectral evaluation of the fluid velocity field at the center of the particle, which involves summing the Fourier-Chebyshev series.

### 2.3 Simulation Parameters

The results presented in this paper are relative to a shear Reynolds number of  $Re_\tau = 150$  based on the shear velocity  $u_\tau = 0.11775 \text{ m s}^{-1}$ . The corresponding average (bulk) Reynolds number is  $Re_b = 2100$ , where  $u_b = 1.65 \text{ m s}^{-1}$  is the average (bulk) velocity. The size of the computational domain in wall units is  $L_x^+ \times L_y^+ \times L_z^+ = 1885 \times 942 \times 300$ . This latter has been discretized in physical space with  $128 \times 128 \times 129$  grid points (corresponding to  $128 \times 128$  Fourier modes and to 129 Chebyshev coefficients in the wave space). This is the minimum number of grid points required in each direction to ensure that the grid spacing is always smaller than the smallest flow scale and that the requirements imposed by the point-particle approach are satisfied. Indeed, in the present flow configuration, the non-dimensional Kolmogorov length-scale,  $\eta_K^+$ , varies along the wall-normal direction from a minimum value  $\eta_K^+ = 1.6$  at the wall to a maximum value  $\eta_K^+ = 3.6$  at the centerline (see Fig.2.1(a)).

The grid resolution in the wall-normal direction is such that the first collocation point is at  $z^+ = 0.05$  from the wall, while in the center of the channel  $\Delta z^+ = 3.7$  [22]. Assuming that particle motions due to strain are negligible, the two requirements explained above deal primarily with the size of the particle, which has to be much smaller than the grid cell to cope with the fact that the velocity  $\mathbf{u}$  used in Eq.2.6 is the (undisturbed) fluid velocity at the center of the particle. Since this velocity is obtained by interpolation of the fluid velocity in the neighboring points, accurate estimate requires that the grid cell is significantly larger than the particle. The accuracy of the fluid flow simulation, however, requires a grid cell significantly smaller than the fluid scales one wants to solve: if the particles are much smaller than the smallest relevant flow scales, than the point-particle restriction is satisfied. In the case of DNS, this means that particles must be much smaller than the Kolmogorov length-scale ( $d_p \ll \eta_K$ ). In one-way coupling simulations, violation of the above restrictions on particle size may introduce significant errors. For heavy particles in gas flows ( $\rho_p/\rho_f \gg 1$ ), however, the time scale of the particles is significantly larger than the time scale of the small scales of the fluid: due to their inertia, the

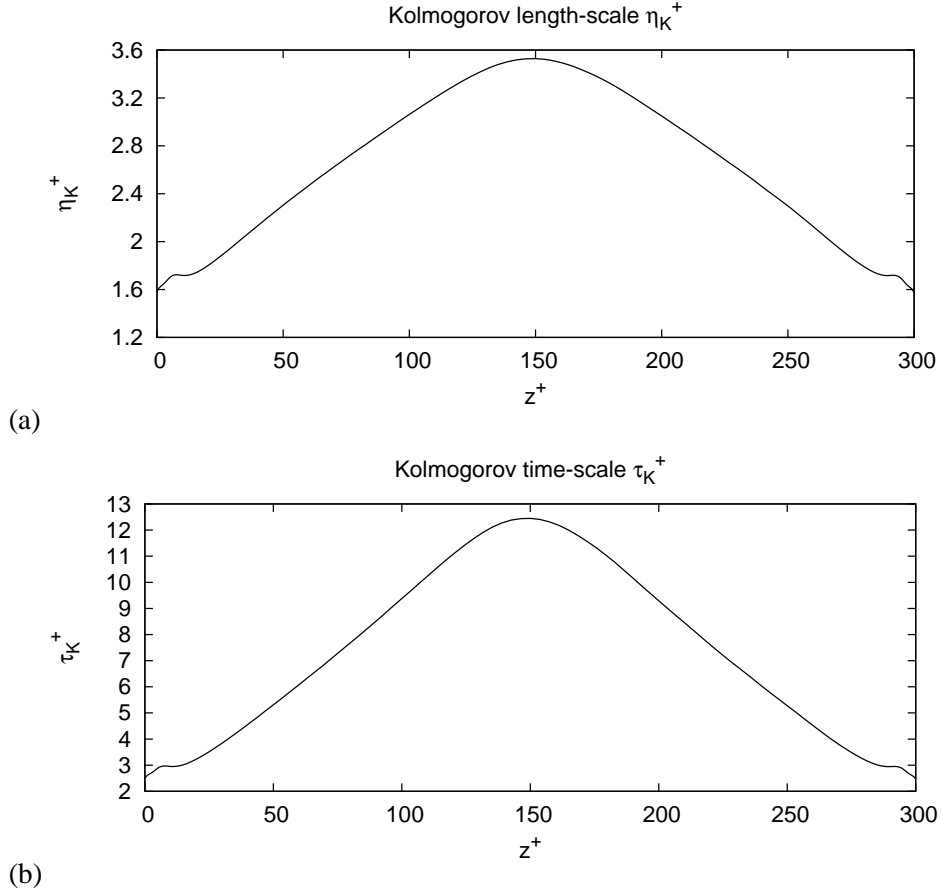


Figure 2.1: The Kolmogorov length-scale  $\eta_K^+$  (a) and time-scale  $\tau_K^+$  (b) as a function of the wall-normal coordinate  $z^+$  in the channel flow at  $Re_\tau = 150$ .

particles act as low-pass filters and are driven mostly by the large scales. The error introduced by a small grid cell is not important and may be neglected, the only consequence being that the particles experience a local flow field with smaller scales than the ones that are forcing the actual particles.

For the simulation, large samples of particles characterized by different response times were considered. The response time is made dimensionless using wall variables, and the Stokes number for each particle set is thus obtained as  $St = \tau_p^+ = \tau_p/\tau_f$ , where  $\tau_f = \nu/u_\tau^2$  is the viscous timescale of the flow. This characteristic time scale is proportional to the turnover time of the turbulent eddies and it supplies a measure of the time available for eddy-particle interaction. In this work we use inertial particles with three different magnitude:  $St = 5, 25$  and  $125$ . We remark that the characteristic timescale of the flow changes depending on the specific value of the shear Reynolds number, namely on the specific value of the shear velocity. In the present case, we have

$\tau_f = 1.13 \cdot 10^{-3} s$ . The non-dimensional value of the Kolmogorov time-scale,  $\tau_K^+$ , ranges from 2.5 wall units at the wall to 12.5 wall units at the channel centerline [22] (see Fig.2.1(b)).

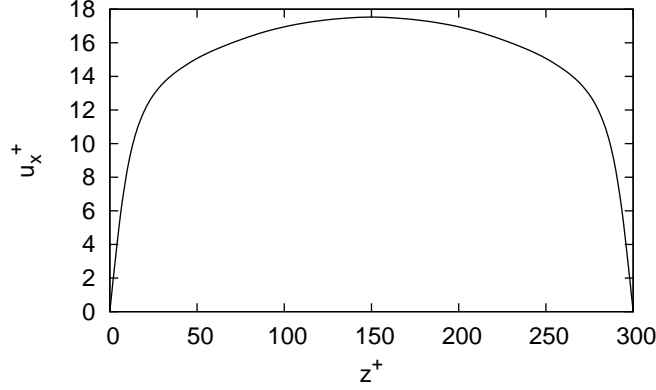


Figure 2.2: The streamwise fluid velocity profile in the turbulent channel flow at  $Re_\tau = 150$ .

Finally, we need a unit of time of the process in order to show the behavior of the particles in comparison with the one of the flow. So we define the *crossing time* ( $\tau_{ct}$ ) as the time that the fluid at the center channel (namely at the maximum of the streamwise velocity profile, see Fig.2.2) takes to cross the whole channel along the streamwise direction:

$$\tau_{ct} = \frac{L_x}{u_{max} \cdot dt^+} \simeq \frac{1885}{17.5 \cdot 0.045} \simeq 108 [t^+]. \quad (2.7)$$

As the simulation is carried out for  $900 t^+$ , we can say that it takes  $8,3 \tau_{ct}$ .

## 2.4 Initial pairs arrangement

A single particle has three (translational) degrees of freedom in the three dimensional space. Differently, a pair of (point-)particles has five degrees of freedom in the physical space: three translations and two rotations. Hereafter we will take the orientation of the vector  $\mathbf{d}(t) = \mathbf{d}_1(t) - \mathbf{d}_2(t)$  as the *orientation* of the pair. In homogeneous isotropic turbulence particles pairs are initially placed in the whole domain with random positions and random orientations and all statistics are computed on all pairs, without any distinctions on current or initial arrangement. This is possible because every part of the domain has the same probability to be affected at a certain time by turbulence structures of the all scales. In a channel flow this is no more true, the small-

est and biggest scales being confined in the boundary layers and in the center channel respectively. So we have to take into account of this non-homogeneity of the flow, calculating separate statistics for different regions of the domain or for separate sets of particles. The first one is an *Eulerian* approach and consists in dividing the channel into slabs parallel to the walls and calculating instantaneous separate statistics for each slab, considering only pairs that are inside that slab at that time. This method provides a good understanding of the fluid motions in circumscribed channel's regions but it does not take memory of particle's history. The second one is a *Lagrangian* approach and consists in releasing different sets of pairs in different specific regions of the channel and computing separate statistics for each set, regardless of their instantaneous position. With this method particles are followed along their trajectories and then a better understanding of pairs behaviour is provided. For this reason we decide to use this latter approach in the present study.

Since the unique non-homogeneous direction in the channel flow is the wall normal one, we decide to place particles pairs on planes orthogonal to the  $z$  axes at the beginning of the simulation. The velocity gradient (shear)  $du_x^+/dz^+$  due to the presence of the walls can be used as a measure of non-homogeneity in order to identify wall normal locations at which release the particles. As shown in Fig.2.3, we choose 7 planes of coordinates  $z^+ = 2, 6, 14, 37, 65, 100, 150$ . Initial locations are confined in the bottom half of the channel because of the flow's symmetry with respect to the centerline ( $z^+ = 150$ ). For each plane, we put three sets of pairs, oriented along the streamwise, spanwise and wall normal direction (hereafter set = 1, 2 and 3 respectively), in order to investigate the influence of turbulence structures (fluctuations) and macroscopic quantities (velocity gradient) on initial orientation. For a specific  $z^+$  coordinate of release, we place the first particle of each pair randomly in  $x$  and  $y$  directions and the second particle spaced of one diameter from the first, oriented as just explained. In this way the initial distance of each pair is  $d(0) = 0.34, 0.76$  and  $1.71$  wall units for  $St = 5, 25$  and  $125$  respectively and then pair dispersion starts from the dissipation subrange for each Stokes number (see Fig.2.1(a)).

Another important parameter to be chosen is the number of pairs for each plane necessary not to affect too much statistics. To this aim, we place  $n_p$  pairs on each plane and we run 4 times a *test* simulation for 1 crossing time ( $t^+/\tau_{ct} = 1$ ), using 4 different initial displacements (due to the random distribution in  $x$  and  $y$  directions). We calculate the mean pair distance  $\langle d(t) \rangle$  for each simulation and then we compute the mean of this four measures,  $\overline{\langle d(t) \rangle}$ , in

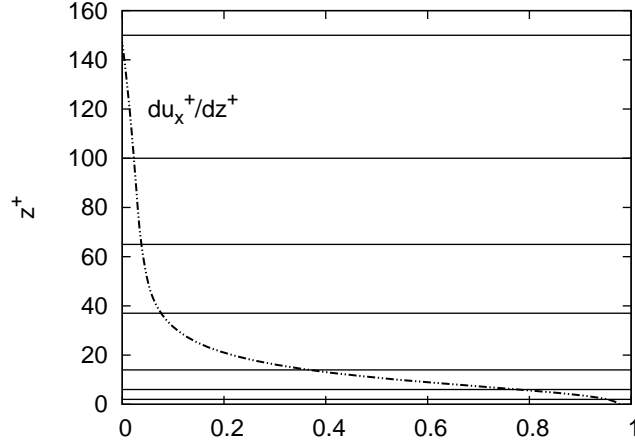


Figure 2.3: The particles pairs are initially placed on 7 planes parallel to the walls in the bottom half of the channel, oriented along the streamwise (set = 1), spanwise (set = 2) and wall normal (set = 3) directions. The velocity gradient (shear) is used as a measure of non-homogeneity along the wall normal direction.

order to have the root mean square of the four tests:

$$\sigma_u = \frac{1}{4} \sum_{i=1}^4 \left( \langle d \rangle_i - \overline{\langle d \rangle} \right)^2. \quad (2.8)$$

We find that for  $n_p = 25000$ ,  $\sigma_u \cdot 100 / \overline{\langle d \rangle}$ , namely the relative statistic error due to the finite number of particles, remains under 5% during the first crossing time (Fig.2.4). So this number of particles seems to be large enough not to affect too much pair statistics. Conservatively, we decide to use a number of particles 4 times larger in our simulations, then we track 100000 pairs for each plane.

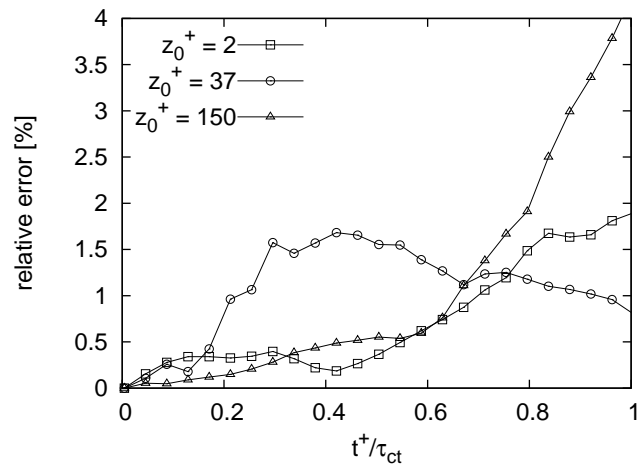


Figure 2.4: The relative statistic error,  $\sigma_u/\langle d \rangle$  [%].



# Chapter 3

## Results and Discussion

### 3.1 Single-particle Statistics

#### 3.1.1 PDF of Single-particle Position

The main purpose of this section is to present single particle statistics of inertial particles. Indeed, the first step to understand the behavior of the system described above is to know the particles positions history of each set during the simulation. First of all we show some snapshots of particles positions at different times, in order to give a qualitative idea of the dispersion process. We choose the two sets with initial wall normal location  $z_0^+ = 2$  and  $z_0^+ = 150$  (Fig.3.1 and 3.2).

Since we want also a quantitative measure of the phenomenon, we compute the single particle position Probability Density Function (PDF) along wall normal direction for different times, namely the probability of a particle to be at a certain  $z^+$  coordinate. PDF displays the instantaneous distribution of each swarm, concentrated on a  $x - y$  plane at the beginning of the simulation. This is the most basic tool to check particles dispersion into the channel.

Fig.3.3 shows the PDF at different crossing times respectively for the planes at initial positions  $z_0^+ = 150$  (center channel),  $z_0^+ = 37$  and  $z_0^+ = 2$  (close to the wall). PDFs displayed refer to  $St = 25$ . The trends for particles with different inertia are similar to these (see Fig.3.4). PDFs shown in figures are related to the set of pairs initially orientated along streamwise direction. Those related to the other 2 sets (along spanwise and wall normal directions) are very similar to these. This is because first particles positions of each pair are the same for all three sets, and second particles positions are very close to each other, maximum at the distance of a particle diameter, that is very small compared to the channel dimensions.

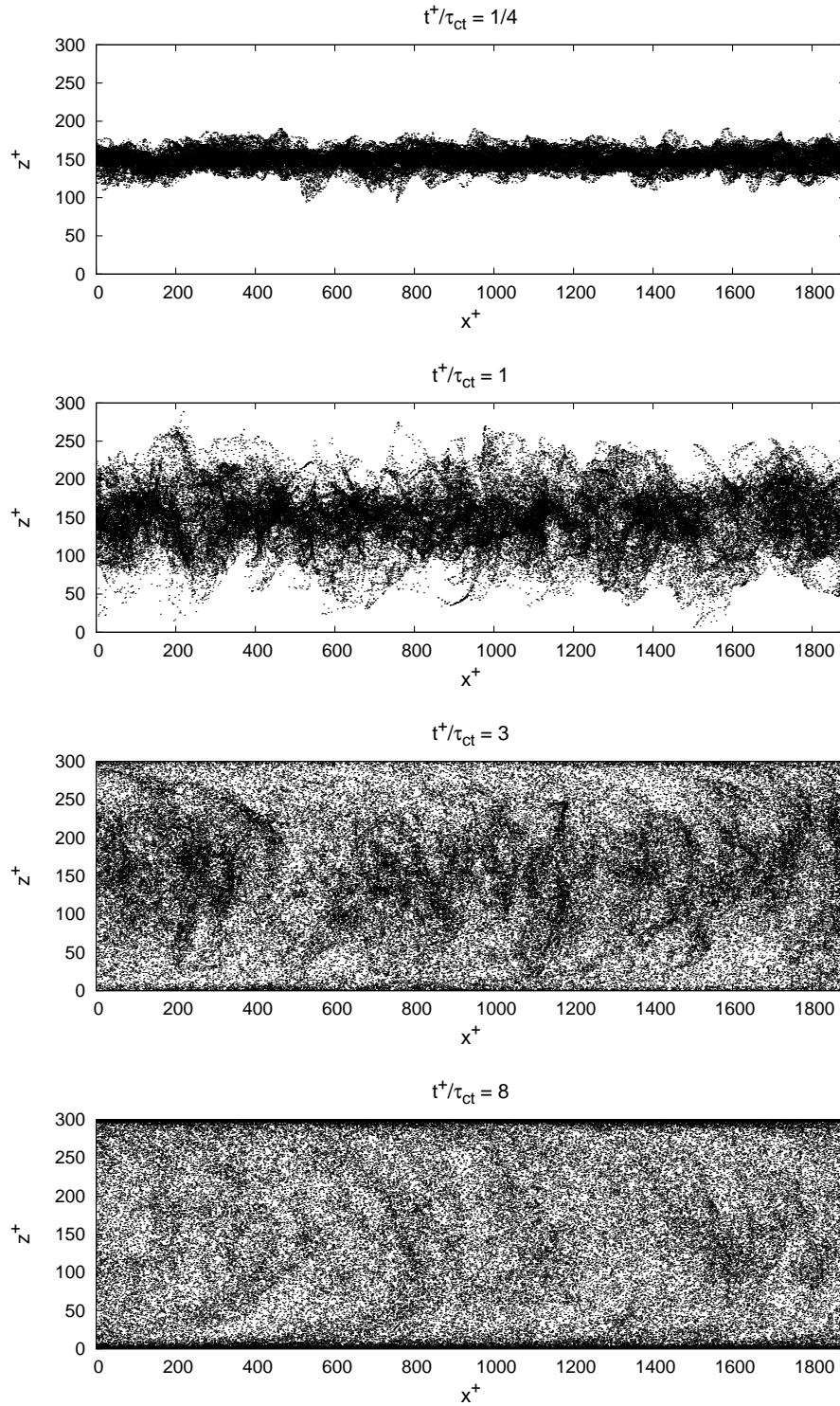


Figure 3.1: Some snapshots of particles instantaneous distribution at several crossing times ( $t^+/\tau_{ct} = 1/4, 1, 3, 8$ ). Particles are released on a plane at  $z_0^+ = 150$  (center of the channel).  $St = 25$ .

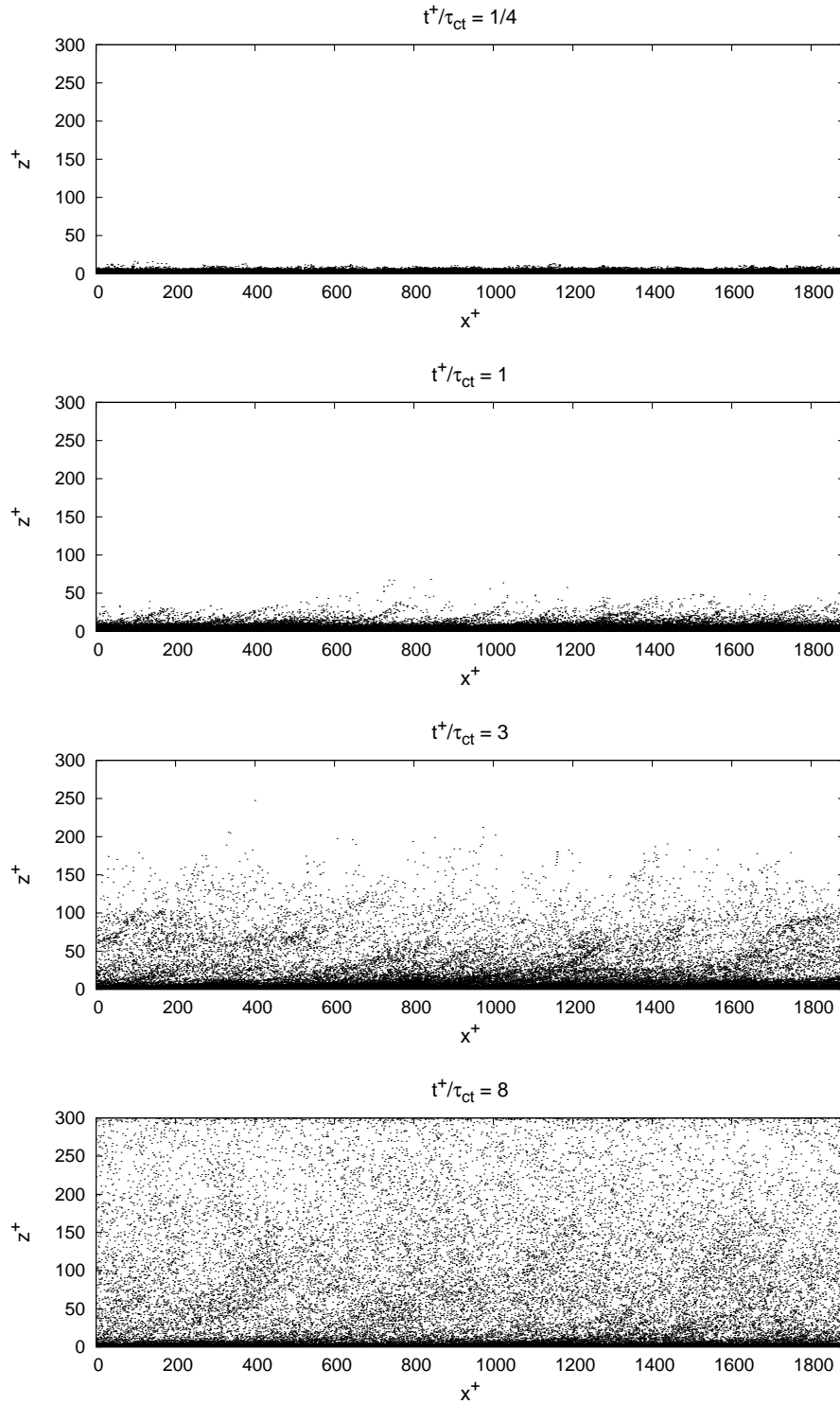


Figure 3.2: Some snapshots of particles instantaneous distribution at several crossing times ( $t^+/\tau_{ct} = 1/4, 1, 3, 8$ ). Particles are released on a plane at  $z_0^+ = 2$  (near the wall).  $St = 25$ .

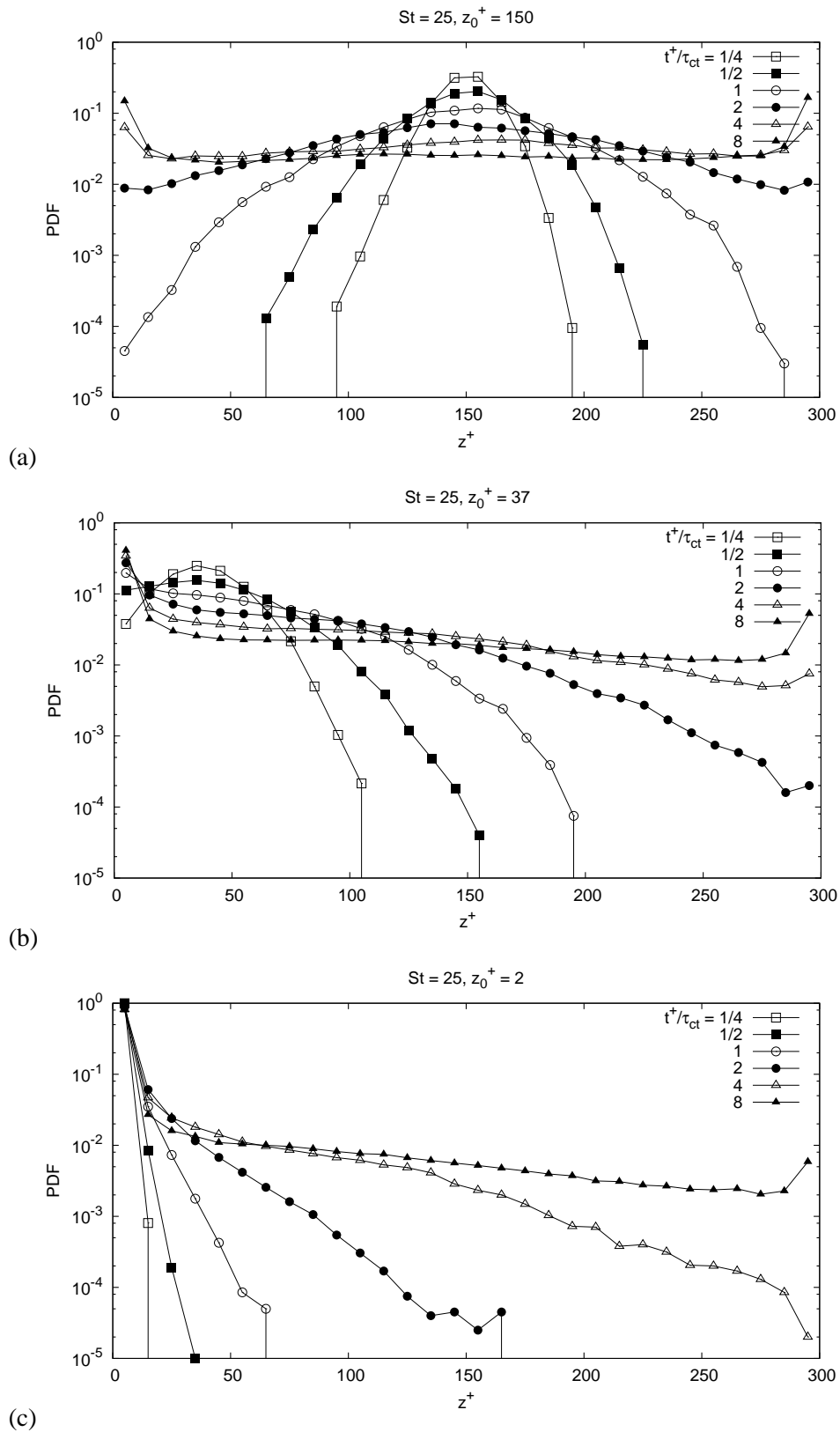


Figure 3.3: Single-particle position PDF at several crossing times for particles released on a plane at  $z_0^+ = 150$  (a),  $z_0^+ = 37$  (b) and  $z_0^+ = 2$  (c).

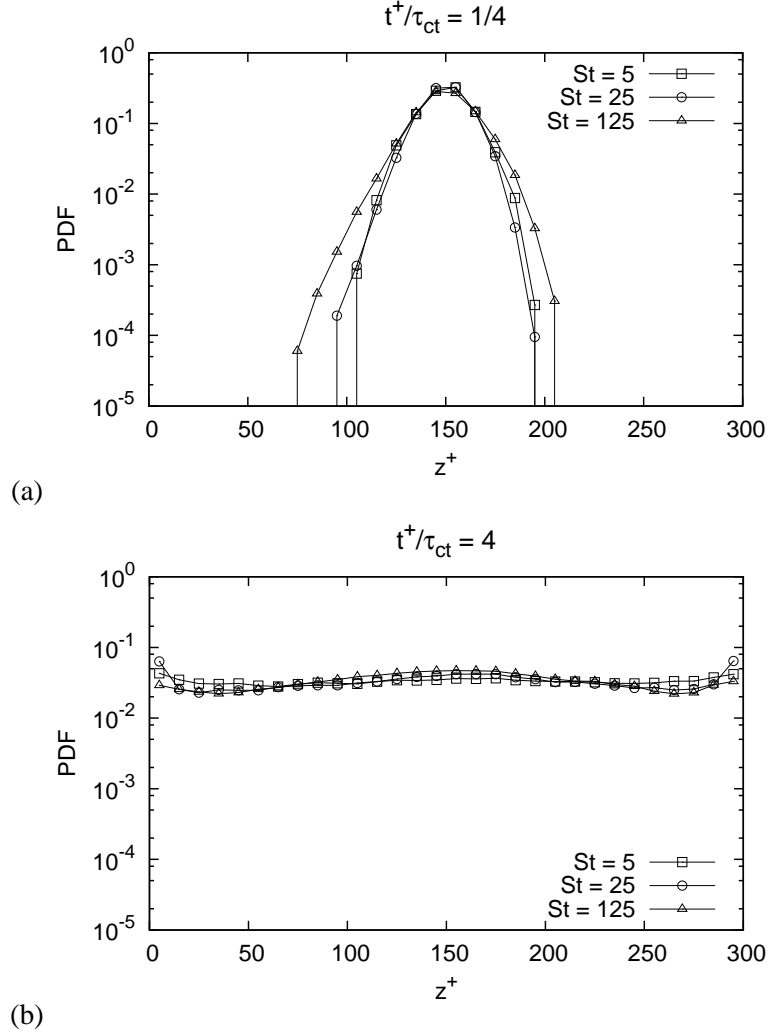


Figure 3.4: The PDFs for  $St = 5, 25$  and  $125$  at  $t^+/\tau_{ct} = 1/4$  (a) and  $4$  (b). Particles distribution is almost the same for the three different particle sizes, especially at large times (b). An optimum for the segregation rate at the walls is found for  $St = 25$ . Particles are originally placed at  $z_0^+ = 150$ .

In Fig.3.3(a) we can see how particles released in the center of the channel move as in a diffusion phenomenon, observable from the parabolic shape of the PDF for  $0 < t^+/\tau_{ct} < 1$  in log scale. After  $t^+/\tau_{ct} = 2 - 4$ , PDF is almost flat along wall normal direction, which means that particles distribution is very homogenous. After  $t^+/\tau_{ct} = 8$  a significant wall segregation is appreciated. From Fig.3.3(c) we can notice that particles released on a plane close to the wall move in a different way. Most of them remain very close to the wall for a long period, while a small quantity of particles moves slowly to the other wall.

After  $t^+/\tau_{ct} = 8$  most of the particles are still near the original  $z^+$  coordinate, so distribution along wall normal direction is very nonhomogeneous. Finally, Fig.3.3(c) shows that particles released on an intermediate plane between a wall and the center channel have a mixed behavior between the two previous cases. Initially a diffusion phenomenon is appreciated around the  $z^+$  coordinate of release. Later most of particles move to the nearest wall and they start there a segregation. Other particles move to the opposite wall. Finally particles homogeneity is at an intermediate level between the two previous cases.

An parametric model to predict PDF in time may be useful. To this aim it's possible to fit data of every particle set with a specific parametric function and extract a time-dependent law for the parameters. From Fig.3.3 it's clear that data for particles originally placed at the centerline can be well fitted by a gaussian function, because of their symmetric diffusive behavior, while data for particles that start near the wall can be better fitted by an exponential function; this is evident from the linear trend of the PDF's tails in log scale. Instead, it's more difficult to find an appropriate fitting function for the other swarms, because of their mixed behavior between the two previous cases. In the next section we will try to find a parametric model only for the two borderlines,  $z_0^+ = 2, 150$ .

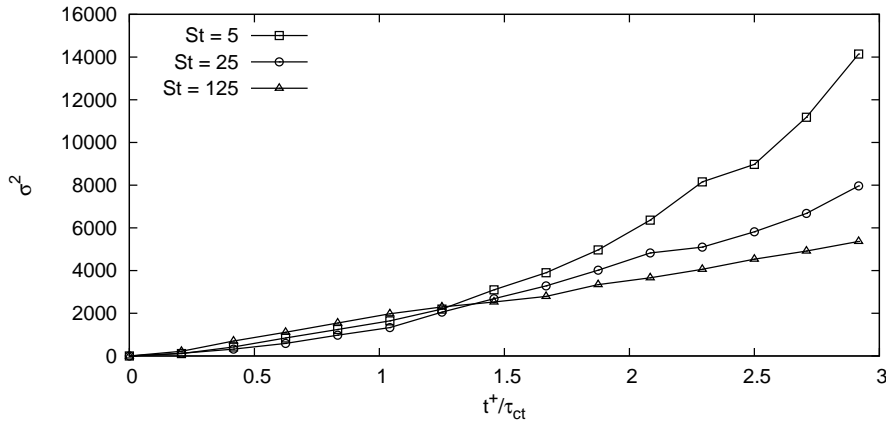


Figure 3.5: The variance of the gaussian distribution is shown for  $1 < t^+/\tau_{ct} < 3$ . Particles are originally placed at  $z_0^+ = 150$ .

### 3.1.2 Parametric Model for Particles Dispersion

#### Particles released at $z_0^+ = 150$

A gaussian function is chosen to fit PDFs of particles originally put at  $z^+ = 150$ :

$$f(x) = \frac{1}{\sqrt{2\pi\sigma^2}} \exp\left[-\frac{(x-\mu)^2}{2\sigma^2}\right]. \quad (3.1)$$

In the previous equation,  $x = t^+/\tau_{ct}$ ,  $\sigma^2$  is the variance and  $\mu$  is the mean value. It's easy to understand that  $\sigma^2$  is necessary and sufficient to describe the phenomenon; in fact, because of its symmetry, the mean value  $\mu$  is always more or less equal to 150. In Fig. 3.5 it's shown the variance for different crossing times. At each time, fit is done only for the range of data belonging to the gaussian distribution, disregarding phenomenon of wall segregation. As we can see, variance increases piecewise linearly, and it reaches an inflection point because of the presence of the walls. After the second crossing time the shape of the PDF departs increasingly from a gaussian function and after the third crossing time no longer makes sense to fit data.

It's interesting to notice the presence of a transient, since the beginning of the simulation until  $t^+/\tau_{ct} = 1.5$ , in which the variance increase rate is almost the same for the three Stokes numbers. This is also observable in Fig. 3.4(a), in which PDFs at  $t^+/\tau_{ct} = 1/4$  for the three different particle sizes is displayed. After that, particle inertia plays a predominant role on the dispersion, this latter becoming the faster the smaller Stokes number. This is because the smaller the particles the better they follow the small vortices, which carry them from the center region of the channel to the walls (turbophoresis process). Once reached the walls, there's an optimum for the segregation rate, which is found to be the highest for  $St = 25$ , according with previous studies (see Fig.3.4(b)). This is because particles with  $St = 25$  have a relaxation time of the same order of the fluid time scale near the walls, so they follow best the structures in the boundary layer and they are trapped near the wall more than the others.

Finally, we fitted the variance's trends, in order to get a parametric model for the dispersion process. Fit is done using a piecewise linear function for each Stokes. In this way the separation between the initial transient and the faster regime of dispersion is pointed out.

### Particles released at $z_0^+ = 2$

If we chose a gaussian function to fit data for the set starting from the centerline, we surely need a different one for particles released near to the wall. Indeed, as mentioned above, most of this latter group of particles remains at a  $z^+$  coordinate very close to the initial one. They are as trapped in a tank in the boundary layer that releases a little quantity of particles at a time in the channel. Linear trends of PDF's tails in log scale suggest us to use an exponential

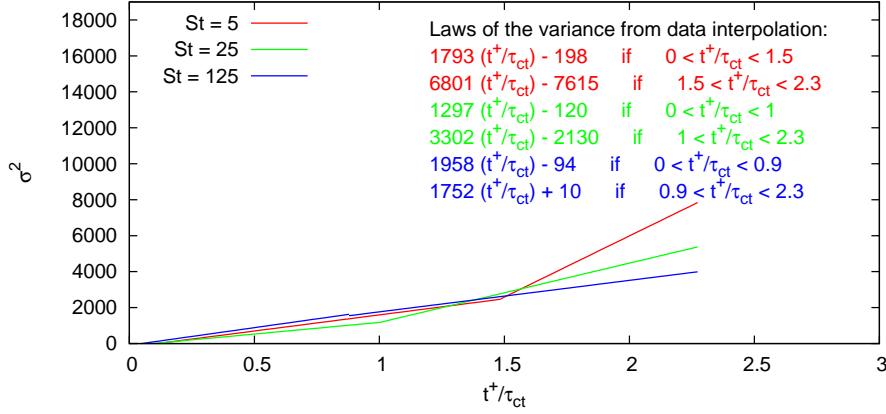


Figure 3.6: A simple model for the law of the variance is obtained by a linear interpolation of the trend of  $\sigma^2$  for  $1 < t^+/\tau_{ct} < 2.3$ . Particles are originally placed at  $z_0^+ = 150$  (gaussian distribution).

function for the fit:

$$f(x) = k \cdot \exp[-x/T]. \quad (3.2)$$

In the previous equation  $x = t^+/\tau_{ct}$ . Also here, at each time fit is done only for the range of data belonging to the exponential distribution, disregarding phenomenon of wall segregation. We make this choice in order to predict with a very simple model particle dispersion from the boundary layer to the rest of the channel. Unlike the previous case, here we need both parameters  $k$  and  $T$  to build the model.

In this case PDF's trend is exponential until the end of the simulation, so we fit data from  $t^+/\tau_{ct} = 1$  to 8. In Fig. 3.7 values of  $T$  and  $k$  obtained from PDF's fit are shown together with their fits in time.  $T$  is a measure of the slope of PDF's tail in log scale: the bigger  $T$  the lower the slope. The value of  $T$  is more or less the same for the three Stokes numbers up to  $t^+/\tau_{ct} = 2$ . This is also observable in Fig. 3.9, in which the PDF at  $t^+/\tau_{ct} = 1$  for the three different particle sizes is displayed. After that, particle inertia plays a predominant role on the dispersion, this latter becoming the faster for  $St = 25$ . In fact, as explained above, this kind of particles follows best the small vortices in the boundary layer and then they are more easily injected in the center of the channel. We notice how the three values of  $k$  converge within  $t^+/\tau_{ct} = 4$ . So, fixed the time (after  $t^+/\tau_{ct} = 4$ ), the main difference between the three cases is the value of  $T$ : the bigger  $T$  the lower the slope (see Fig. 3.8), the greater particle omogeneity along wall normal direction, the

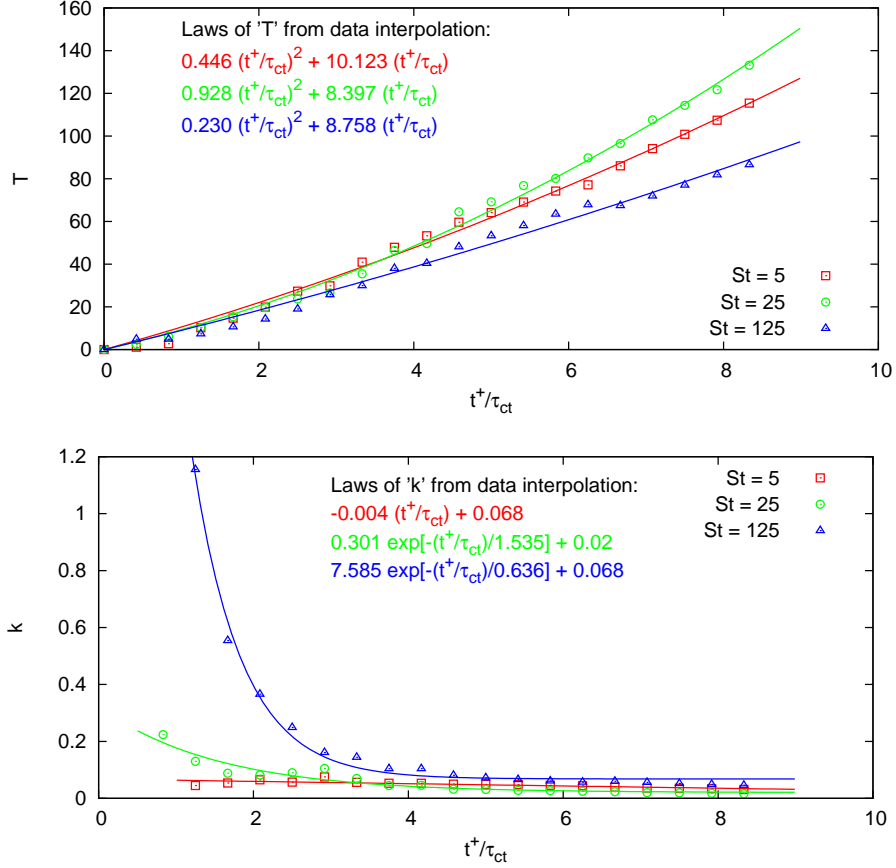


Figure 3.7: Data of  $T$  and  $k$  and relative time-dependent laws obtained by interpolation are displayed. Particles are released at  $z_0^+ = 2$  (exponential distribution).

greater particle concentration at the second wall. In fact, after an infinite time, we expect a steady state in which most of the particles are entrapped at the two walls - with the same concentration - and only few of them move along the channel at the same rate up and down, keeping the overall homogeneous distribution in the central region. Therefore, PDF tail's slope is a measure of the diffusion rate along  $z^+$  coordinate; with this view we can apply Fick's first law to describe qualitatively the phenomenon. The law relates the diffusive flux to the concentration field, by postulating that the flux goes from regions of high concentration to regions of low concentration, with a magnitude that is proportional to the concentration gradient (spatial derivative):

$$J = -D \frac{\partial \phi}{\partial z}. \quad (3.3)$$

$J$  is the diffusion flux,  $D$  is the diffusion coefficient or diffusivity,  $\phi$  is the

concentration and  $z$  is the position. In this case,  $J$  is the flux of particles along wall normal direction,  $\phi$  is particle concentration at a certain  $z^+$  position and the gradient  $\frac{\partial \phi}{\partial z}$  is related to  $1/T$ , being maximum at the beginning of the simulation and going to zero after an infinite time (see Fig. 3.8). The diffusivity  $D$  is probably related to the Stokes number both the flow characteristics.

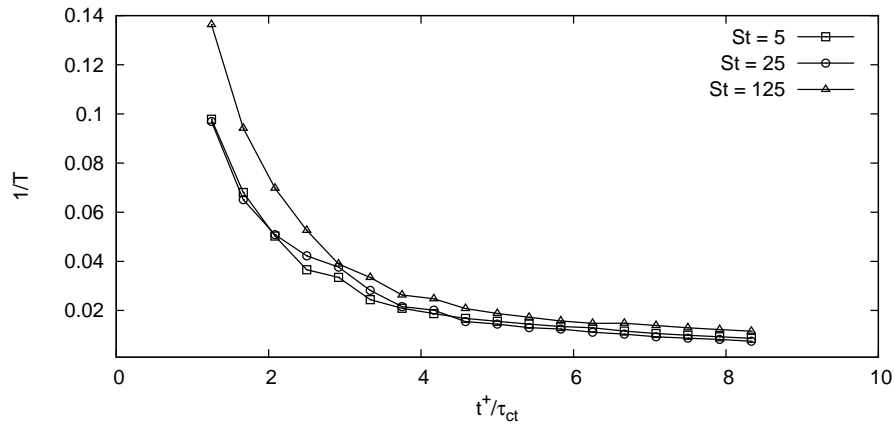


Figure 3.8: The trend of  $1/T$  (values of  $T$  are obtained fitting the PDFs).  $1/T$  is the slope of PDF's tail in logarithmic scale and it's also proportional to the term  $\frac{\partial \phi}{\partial z}$  in Fick's first law. We expect that  $1/T$  goes to zero after an infinite time, which corresponds to an homogeneous particle distribution in the central region of the channel.

Finally, we can notice that at a certain time PDF for  $St = 25$  is lower than the other two in the central region. This accords with the lower value of  $k$  for  $St = 25$  (after  $t^+/\tau_{ct} = 4$ ) and with the maximum of concentration to the walls. This means that this kind of particles tends to stay in the boundary layers rather than in the central region.

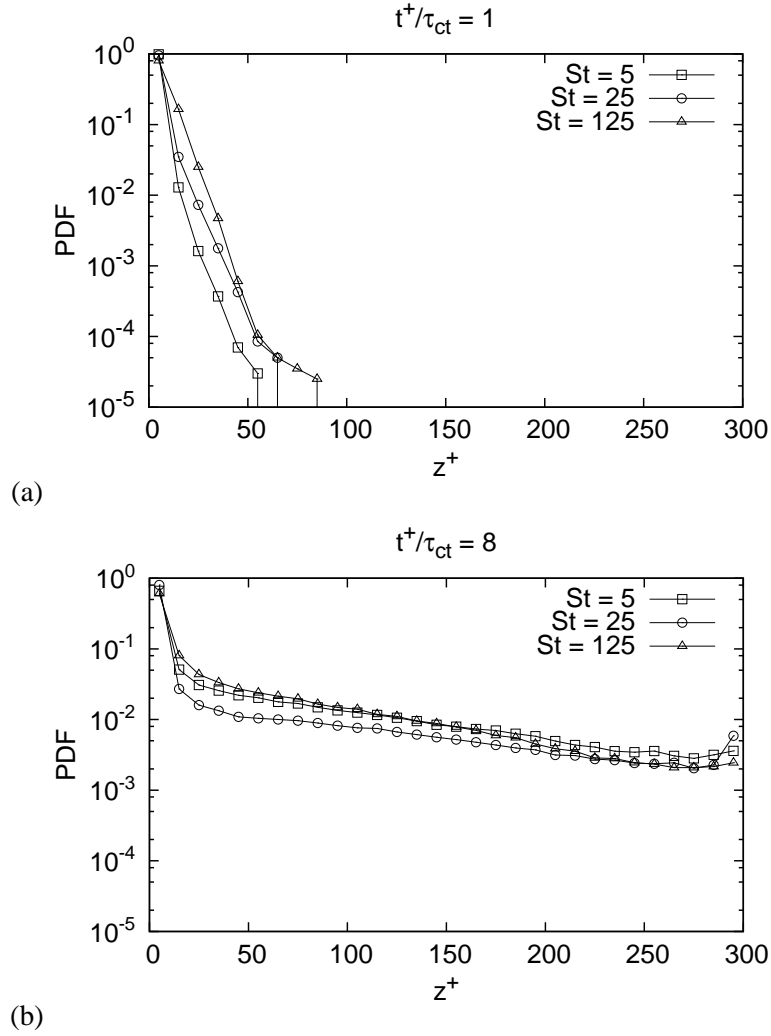


Figure 3.9: Comparison between the PDFs for  $St = 5, 25$  and  $125$ , at two different times. At  $t^+/\tau_{ct} = 1$  (a) the three trends are very similar, while at  $t^+/\tau_{ct} = 8$  (b) a different slope for different Stokes numbers is observed. Particles are originally placed at  $z_0^+ = 2$ .

If we look at the snapshots of Fig. 3.1 and 3.2, we notice a similarity with the pictures of smoke expelled by a chimney and by a fire in Fig. 1.10. In both cases there's an unidirectional strong pressure gradient that drives the second phase (smoke, steam or particles swarms) in the first phase (air) and the presence of a surface (channel walls or ground) influences the flow with a shear.

## 3.2 Pair dispersion

### 3.2.1 Statistics

In this section the pair dispersion statistics are presented. For simplicity we will show results only for  $St = 25$  and then we will discuss any deviations for lighter and heavier particles ( $St = 5$  and  $125$  respectively).

As mentioned in Sec.1.4.1, in isotropic homogenous turbulence Richardson's law predicts the scaling  $\langle d^2(t) \rangle \sim t^3$  in the inertial subrange, where  $d(t)$  is the pair distance at time  $t$ . Thus, the first quantity we plot is the mean square pair distance  $\langle d^2(t) \rangle$  for different initial wall normal locations  $z_0^+$  and different initial orientations (Fig.3.10). In Sec.1.4.1 we defined the inertial subrange such that  $\eta_K \ll d(t) \ll L$ , where  $\eta_K \equiv (v^3/\langle \varepsilon \rangle)^{1/4}$  is the Kolmogorov length-scale and  $L$  is the integral length-scale. We fix upper limit of inertial range at  $L = h = 150$ , that is the half-height of the channel, and it is independent of the initial position of the plane, while lower limit is fixed at  $10 \cdot \eta_K^+$  and it varies along wall normal direction because  $\eta_K^+$  varies. In this way it is possible to show the exponential trend of dispersion into the inertial subrange. To this aim, we chose straight lines of different slopes and plotted them on the same figure.

In Fig.3.11 the variance  $\sigma^2 = \sum_{i=1}^N (d_i - \langle d \rangle)^2 / N$  is used as error bar to quantify deviation of separation of each pair from the mean value,  $N$  being the number of pairs for each set.

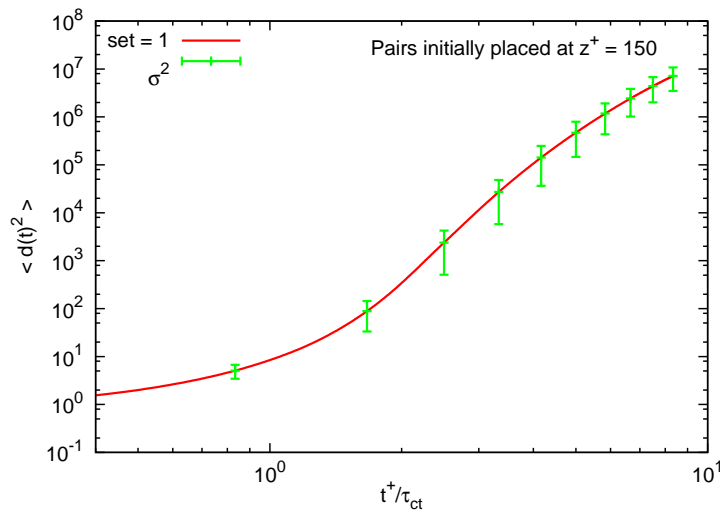


Figure 3.11: The variance  $\sigma^2 = \sum_{i=1}^N (d_i - \langle d \rangle)^2 / N$  is used as error bar to quantify the deviation of separation of each pair from the mean value.

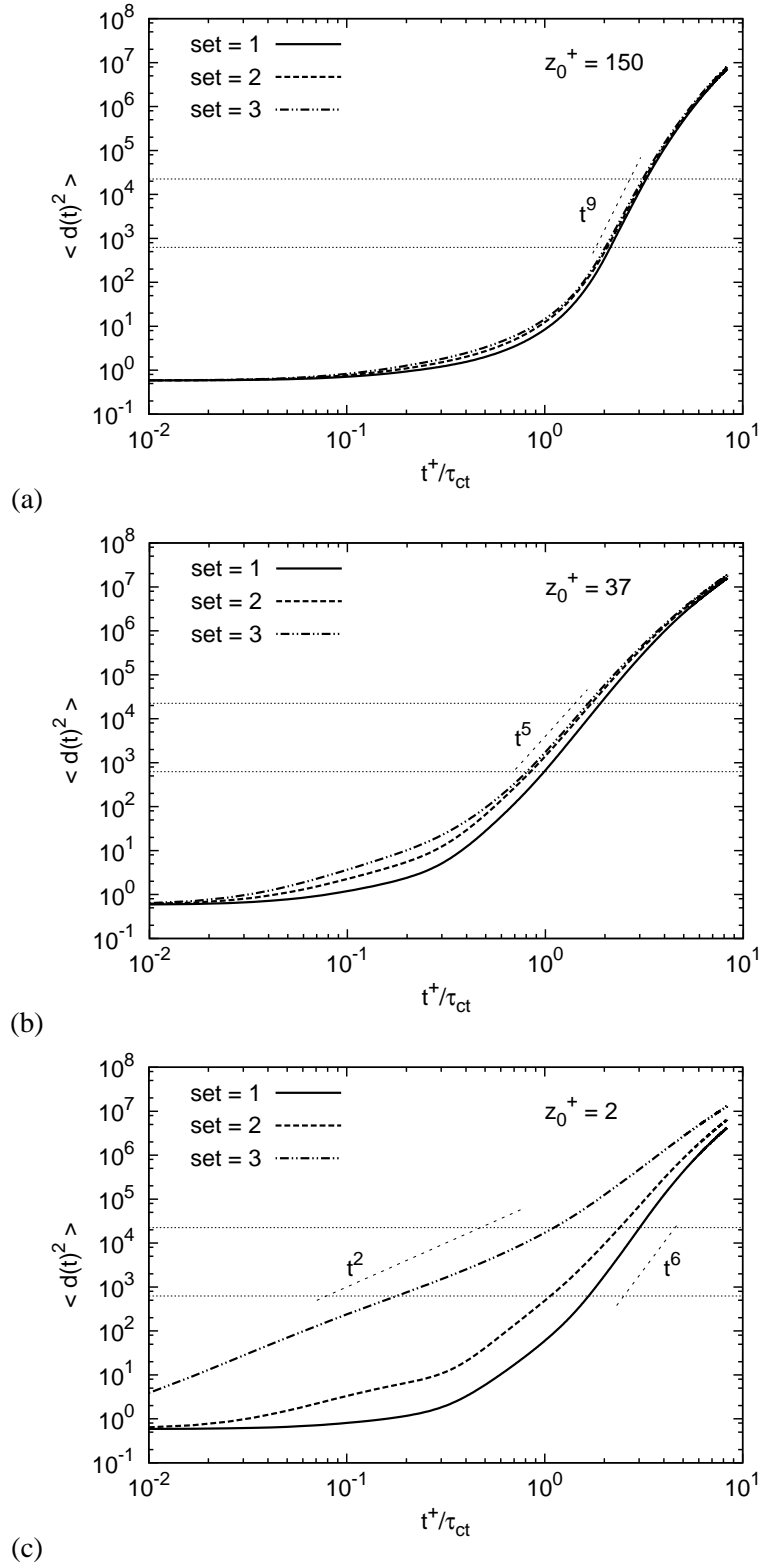


Figure 3.10: The evolution of the mean square pair distance  $\langle d^2(t) \rangle$  for particles pairs released at  $z_0^+ = 150$ , (center of the channel),  $z_0^+ = 37$  and  $z_0^+ = 2$  (close to the wall) oriented along the streamwise, spanwise and wall normal direction respectively (set = 1, 2 and 3). Stokes number = 25 (intermediate size). Slopes are plotted just as trendlines (no data fit) in the inertial range (located between the horizontal lines).

In Fig.3.12 a comparison between  $St = 5, 25$  and  $125$  is shown for pairs initially oriented along streamwise direction. In general, particles with  $St = 125$  separate slower than those with  $St = 25$ , while lighter ones separate at the same speed or faster (see trendlines in the figure).

Since some pairs separate rapidly while others remain close together, slowly separating pairs (which remain in the dissipative subrange) and rapidly separating pairs (which approach the integral scales) *contaminate* the statistics in the inertial subrange. To disentangle the effects of different scales, an alternative approach, based on *exit time* statistics, has been proposed [2]. This consists of fixing a set of thresholds,  $d_n = \rho^n d_0$ , where  $\rho > 1$  and  $n = 1, 2, 3, \dots$ , and then calculating the time  $T$  taken for the pair separation to change from  $d_n$  to  $d_{n+1}$ . By averaging over the particle pairs, we obtain the mean exit time,  $\langle T_\rho(d_n) \rangle$ , or mean *doubling time* if  $\rho = 2$ . Formally, we are calculating the first passage time. The advantage of this approach is that all pairs are sampled at the same scales and that finite Reynolds number effects are less important. In Fig.3.13 the exit time statistics calculated with this method are shown.

In Fig.3.14 we show the time  $T$  taken for the pair separation to change from  $d_0$  to  $d_{n+1}$ . We name  $T$  the *total exit time*, to distinguish it from the previous statistic. For each figure we draw the trendlines for the inertial subrange; these latter are proportional to  $d^{2/\alpha}$ ,  $\alpha$  being the exponent we chose for the slopes in Fig.3.10. We also show the straight line proportional to  $d^{2/3}$ , which corresponds to Richardson's law, and that one proportional to  $d$  for set 3 at small times near the wall. Finally, in Fig.3.15 the total mean exit time for particles with  $St = 125$  is shown, together with the straight line proportional to  $d^{2/6}$ . As evident from the good agreement between dispersion trends and trendlines, this latter statistic confirm very well results obtained from the first one (Fig.3.10).

We now consider the statistics of the relative velocity of the particle pairs during the separation process and which we denote as  $\mathbf{u}_r(t) = \mathbf{u}_1(t) - \mathbf{u}_2(t)$ . The relative velocity statistics are of interest because they provide information on the rate of separation of the particle pairs. We consider the statistics of the relative velocity projected in the direction of the separation vector, the *longitudinal* component. The former is given by

$$u_{||} = \frac{d}{dt} [d(t)] = \mathbf{u}_r \cdot \hat{\mathbf{d}}, \quad (3.4)$$

where  $\hat{\mathbf{d}} = \mathbf{d}/d$ . Following the exit time method described above, we calculate the relative velocity at fixed scales in order to achieve *uncontaminated* inertial subrange statistics and which we term the *exit velocities*. We compute

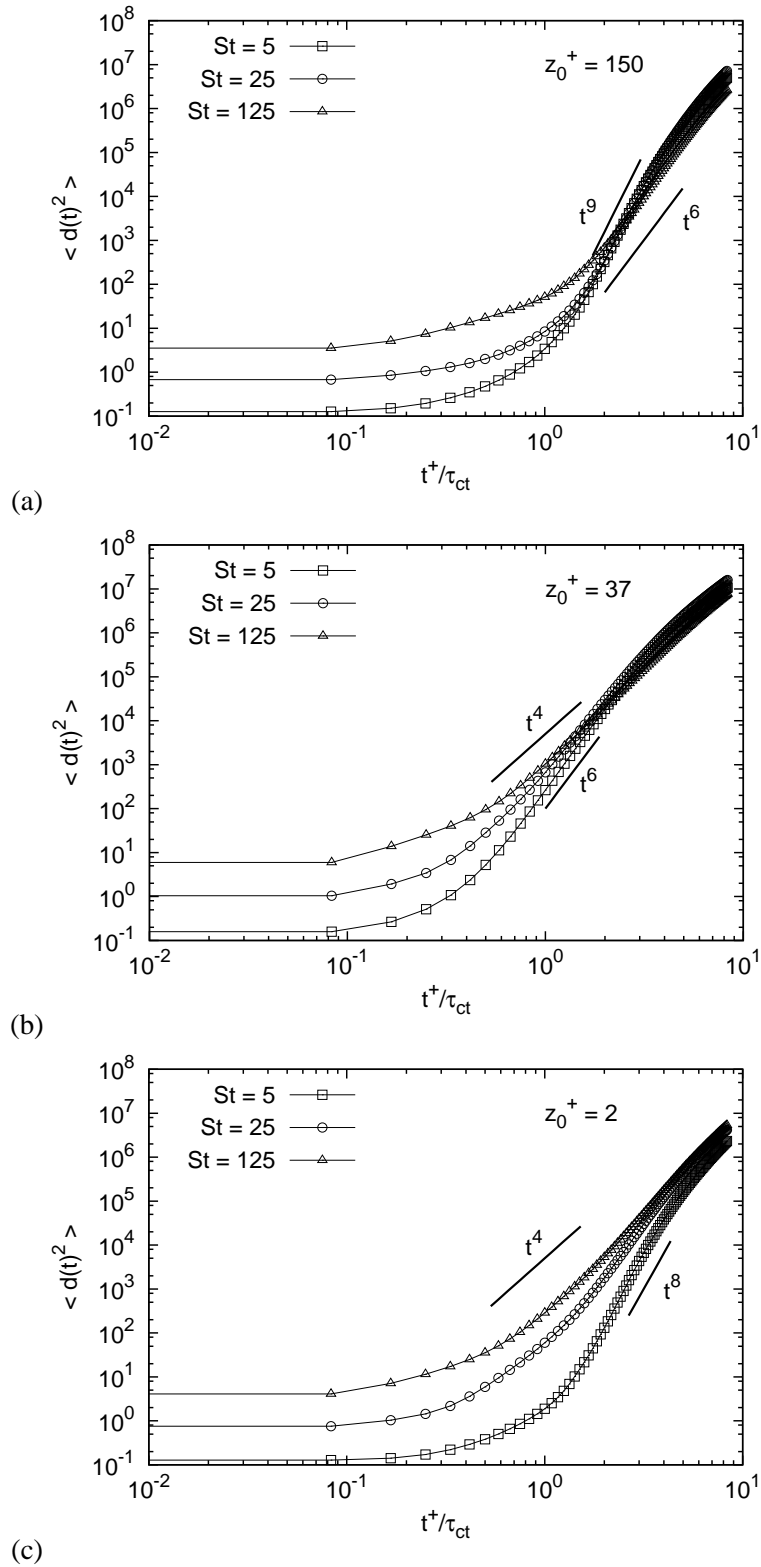


Figure 3.12: The evolution of the mean square pair distance  $\langle d^2(t) \rangle$  for particles pairs released at  $z_0^+ = 150$ , (center of the channel),  $z_0^+ = 37$  and  $z_0^+ = 2$  (close to the wall) oriented along the streamwise direction. Comparison between  $St = 5, 25$  and  $125$ . Slopes are plotted just as trendlines (no data fit) in the inertial range.

the value of the relative velocity component  $u_{||}(d)$  whenever a particle pair has a separation within a specified logarithmic shell of radius  $d = d_n(1 \pm 0.1)$ , with  $d_n = \rho^n d_0$ . This differs from the method we used to calculate the exit times above as here we are calculating not just the velocity at the first passage but also at all subsequent passages. In Fig.3.16 we plot the mean longitudinal exit velocity,  $\langle u_{||}(d) \rangle$  as a function of the absolute separation  $d$ .

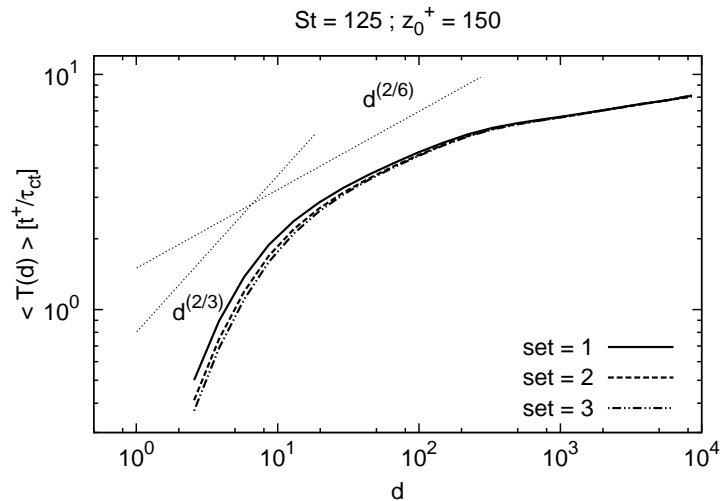


Figure 3.15: The *total mean exit time*  $\langle T(d) \rangle$  for pairs released at  $z_0^+ = 150$  oriented along the streamwise, spanwise and wall normal direction respectively (set = 1, 2 and 3). Stokes number = 125;  $\rho = 1.5$ . Slopes are plotted just as trendlines (no data fit).

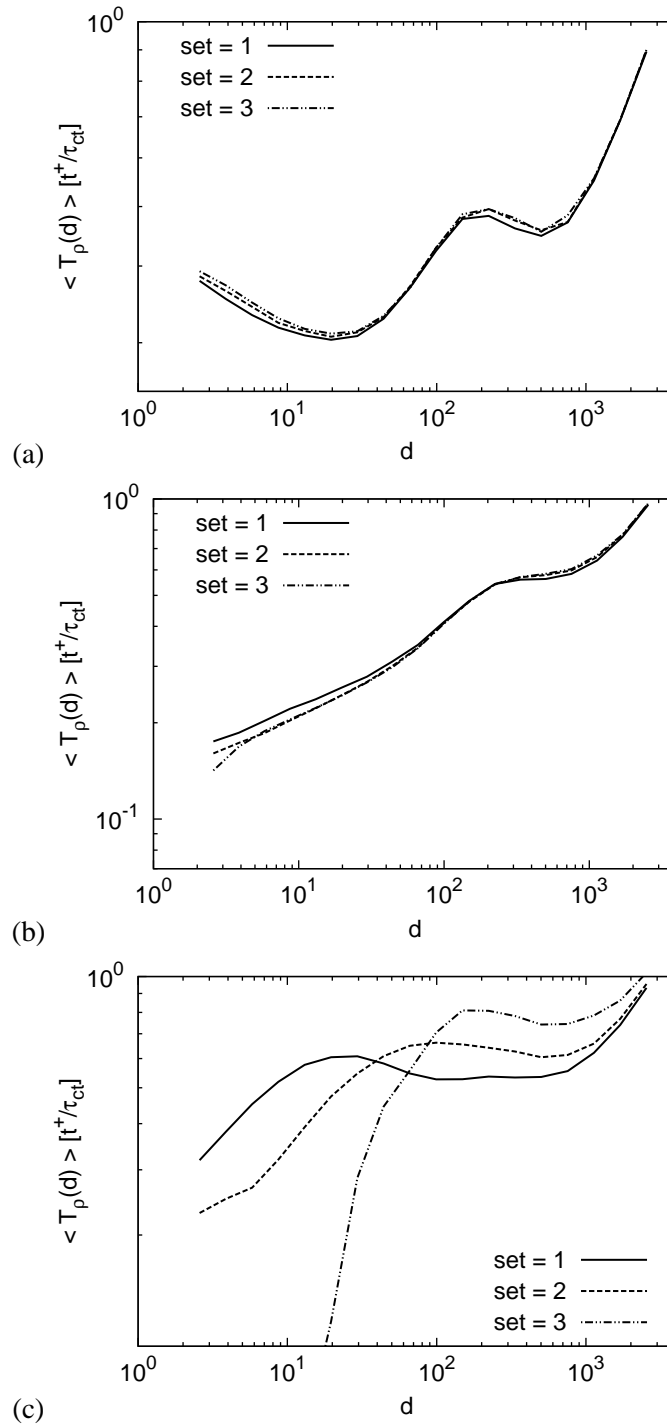


Figure 3.13: The mean exit time  $\langle T_p(d) \rangle$  for pairs released at  $z_0^+ = 150$ , (center of the channel),  $z_0^+ = 37$  and  $z_0^+ = 2$  (close to the wall) oriented along the streamwise, spanwise and wall normal direction respectively (set = 1, 2 and 3). Stokes number = 25 (intermediate size);  $\rho = 1.5$ .

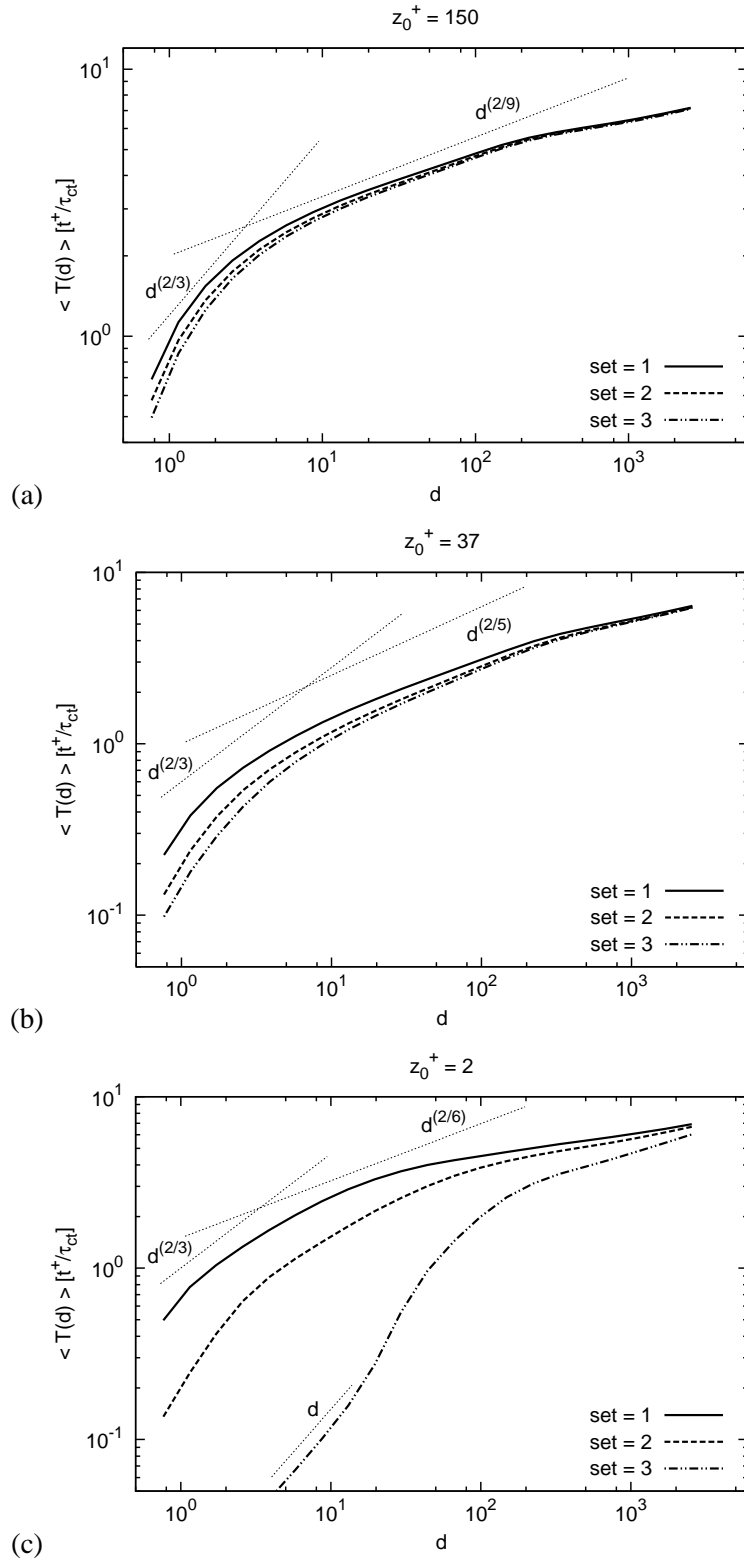


Figure 3.14: The total mean exit time for pairs released at  $z_0^+ = 150$ , (center of the channel),  $z_0^+ = 37$  and  $z_0^+ = 2$  (close to the wall) oriented along the streamwise, spanwise and wall normal direction respectively (set = 1, 2 and 3). Stokes number = 25 (intermediate size);  $\rho = 1.5$ . Slopes are plotted just as trendlines (no data fit).

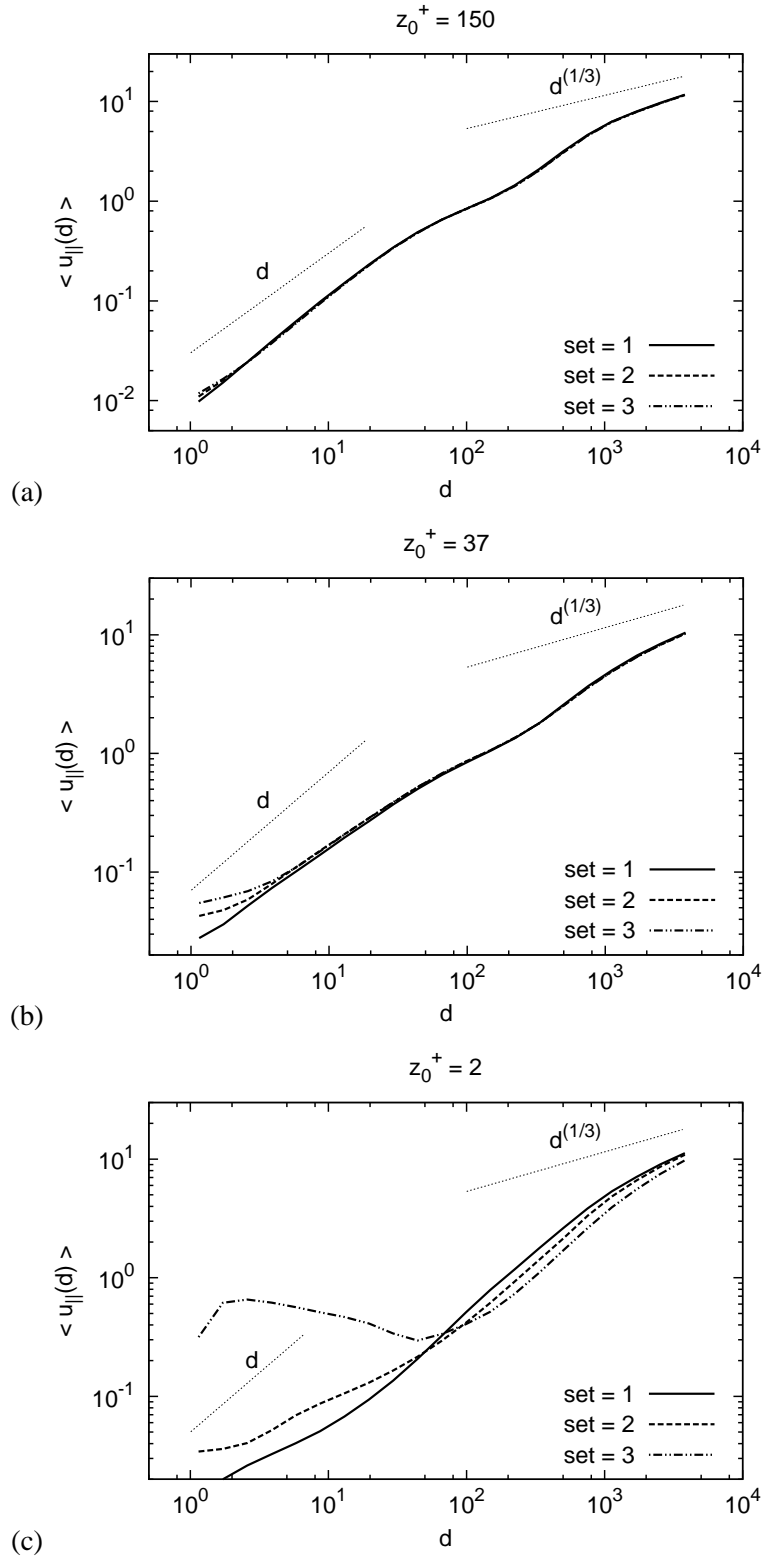


Figure 3.16: The mean longitudinal exit velocity  $\langle u_{||}(d) \rangle$  as a function of the separation  $d$  for pairs released at  $z_0^+ = 150$ , (center of the channel),  $z_0^+ = 37$  and  $z_0^+ = 2$  (close to the wall) oriented along the streamwise, spanwise and wall normal direction respectively (set = 1, 2 and 3). Stokes number = 25 (intermediate size);  $\rho = 1.5$ . Slopes are plotted just as trendlines (no data fit).

### 3.2.2 Discussion

The first observation we do regarding Fig.3.10 is that the slopes of trendlines in the inertial subrange are much steeper than those in homogeneous isotropic turbulence, especially for the swarm initially placed at the centerline ( $z_0^+ = 150$ ). In fact we find a trend proportional to  $t^9$  and not to  $t^3$ , as predicted by Richardson's law. Focusing on this set of particles, we note that they leave the center region and spread to the walls exploring channel's regions with shear's value progressively higher (see Fig.3.17), namely they go through an increasingly nonhomogeneous flow (see also Sec.3.1). Thus, first hypothesis about disagreement with Richardson's law is that the shear somehow increases pair separation. Indeed the main difference between isotropic homogeneous turbulence and the channel flow is that in this latter the shear introduces a new time and length scale in the flow, and consequently also in the scaling of pair dispersion. Here below we qualitatively discuss this effect and we also present several measures in order to quantify the role of the shear compared with that one of turbulence fluctuations on dispersion process.

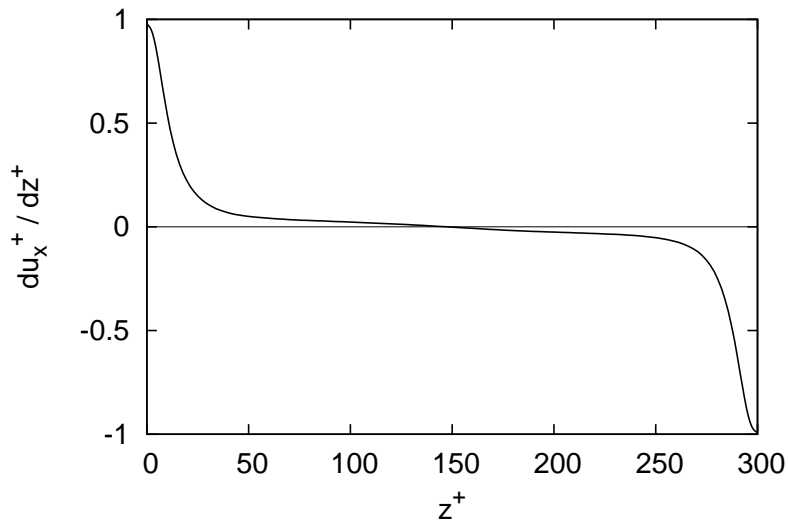


Figure 3.17: The mean shear  $du_x^+ / dz^+$  along the wall normal direction in the channel flow.

Still looking at Fig.3.10, the closer to the wall the location of particles release the more different behavior between set = 1, 2 and 3 is appreciated. For all the cases, pairs of set = 3 separate faster than those of set = 2, and the latter separate faster than those of set = 1. This different behavior can be justified by the different effects of fluid motions on the pairs at the first stages

of simulation. For example, for particles initially placed on a plane at  $z_0^+ = 2$  (close to the wall), pairs initially oriented along wall normal direction are affected above all by the action of the shear and in second order by the effect of the quasi-streamwise counter-rotating vortices which populate the near wall region (see Sec.1.2 for details). Instead pairs initially oriented along spanwise direction are affected only by the effect of the counter-rotating vortices and finally pairs initially oriented along streamwise direction are not affected by any of these two fluid structures, but only by the local turbulence fluctuations. This is no more true for particles released at the centerline (Fig.3.10(a)): here initial orientation affects almost for nothing pair dispersion. In fact, as we can see in Fig.3.17, the greater the distance from the walls the less the shear value, being this latter zero at the centerline. This means that the greater the distance from the walls the more turbulence fluctuations become the only cause of separation and in the center of the channel we expect a particles behavior analogue to that one in homogeneous isotropic turbulence [22].

For pairs released at  $z_0^+ = 150$ , (center channel, Fig.3.10(a)) dispersion trend is proportional to  $t^9$  for all 3 sets, while it decreases to  $t^5$  for the swarm initially placed at  $z_0^+ = 37$  (Fig.3.10(b)). Looking at pairs initially put close to the wall it is evident that the slope is very different for the 3 sets: it goes from  $\sim t^6$  for set = 1 down to  $\sim t^2$  for set = 3 (Fig.3.10(c)). This difference is due to the high shear near the wall, which imposes substantial differences on fluid streamwise velocity also for small increments along wall normal direction. So particles pairs initially oriented along  $z$  axis are affected by the shear from the first instants of simulation. If they were tracers, they follow perfectly the motion of fluid at their positions; for instance, consider two particles spaced of  $\delta$  along  $z$  at time  $t = 0$ . If we call  $S = du_x^+/dz^+$  the shear and  $u_1^+$  and  $u_2^+$  the streamwise fluid velocity components at the two particles positions, then the quadratic pair distance at a certain time  $t = \tilde{t}$  will be:

$$\begin{aligned} d^2(t = \tilde{t}) &= \delta^2 + |u_1^+ \tilde{t} - u_2^+ \tilde{t}|^2 = \delta^2 + [|u_1^+ - u_2^+| \tilde{t}]^2 \\ &\simeq \delta^2 + [(S \cdot \delta) \tilde{t}]^2 \simeq S^2 \delta^2 \tilde{t}^2, \end{aligned} \quad (3.5)$$

where  $S = S|_{z_1^+ \cong z_2^+}$ , with the hypothesis that  $\delta^2 \ll [(S \cdot \delta) \tilde{t}]^2$ . This result is in agreement with the slope  $\sim t^2$  shown in Fig.3.10 just above trend of set = 3. This means that even if in this study we are not tracking tracers but inertial particles, the difference due to drag and inertia forces (the only ones we consider active on the particles) is negligible at the first stages, also because particles

velocities are initialized with fluid velocities at their initial positions. Instead, pairs of set = 1 and 2 are initially affected only by turbulent fluctuations and since shear effect is dominant on these latter for low values of  $z^+$ , this pairs take more time to wander out of alignment from  $x$  and  $y$  axis respectively, so that they can be affected by different values of streamwise velocity and start a faster separation.

From these observations we can infer that the turbulence fluctuations and the shear play two different roles in space and time regarding pair dispersion. According with Richardson's hypothesis, for which eddies of scale  $l \sim d(t)$  are most effective in the process of dispersion, the small fluctuations are responsible of separation above all in the dissipation subrange, while the shear, that is a mean quantity, acts on the bigger scales (inertial subrange) and then it becomes dominant at large time. In Fig.3.18 we plot a comparison between the shear  $du_x^+/dz^+$  and the inverse of the Kolmogorov time-scale  $\tau_K^+$ , in order to show that in the center channel the small turbulence fluctuations are predominant on the shear and vice versa at the walls.

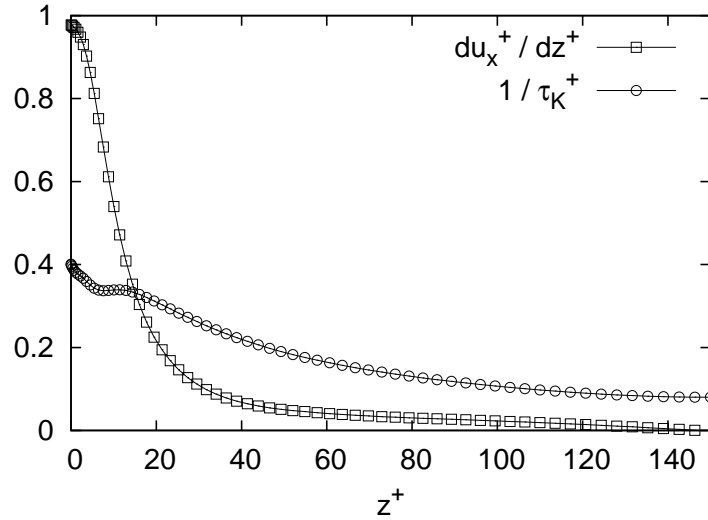


Figure 3.18: Comparison between the shear  $du_x^+/dz^+$  and the inverse of the Kolmogorov time-scale  $\tau_K^+$ . In the center of the channel the small turbulence fluctuations are predominant on the shear and vice versa at the walls.

In Fig.3.19(a) we compare the mean square distance  $\langle d^2 \rangle$  for particles released at  $z_0^+ = 150$  with its three components  $\langle d_x^2 \rangle$ ,  $\langle d_y^2 \rangle$  and  $\langle d_z^2 \rangle$ . At small times ( $t^+/\tau_{ct} < 1$ ), corresponding to the dissipation subrange,  $\langle d_x^2 \rangle \approx \langle d_y^2 \rangle \approx \langle d_z^2 \rangle$ , but at larger times ( $2 < t^+/\tau_{ct} < 3$ ), corresponding to the inertial subrange, we observe that  $\langle d^2 \rangle \approx \langle d_x^2 \rangle \sim t^9$ . This means that most of the pairs have sep-

arated so much that at a certain time the two particles of each pair perceived very different values of streamwise velocity. For instance, the first particle has segregated at a wall while its twin is driven by the flow at center of the channel. Therefore, inertial subrange of turbulence is contaminated by the effect of the shear and the two particles of most of the pairs decorrelate before reaching it. In Fig.3.19(a) particles are released at  $z_0^+ = 150$  oriented along streamwise direction. A similar behavior was found for other wall normal locations and initial orientations.

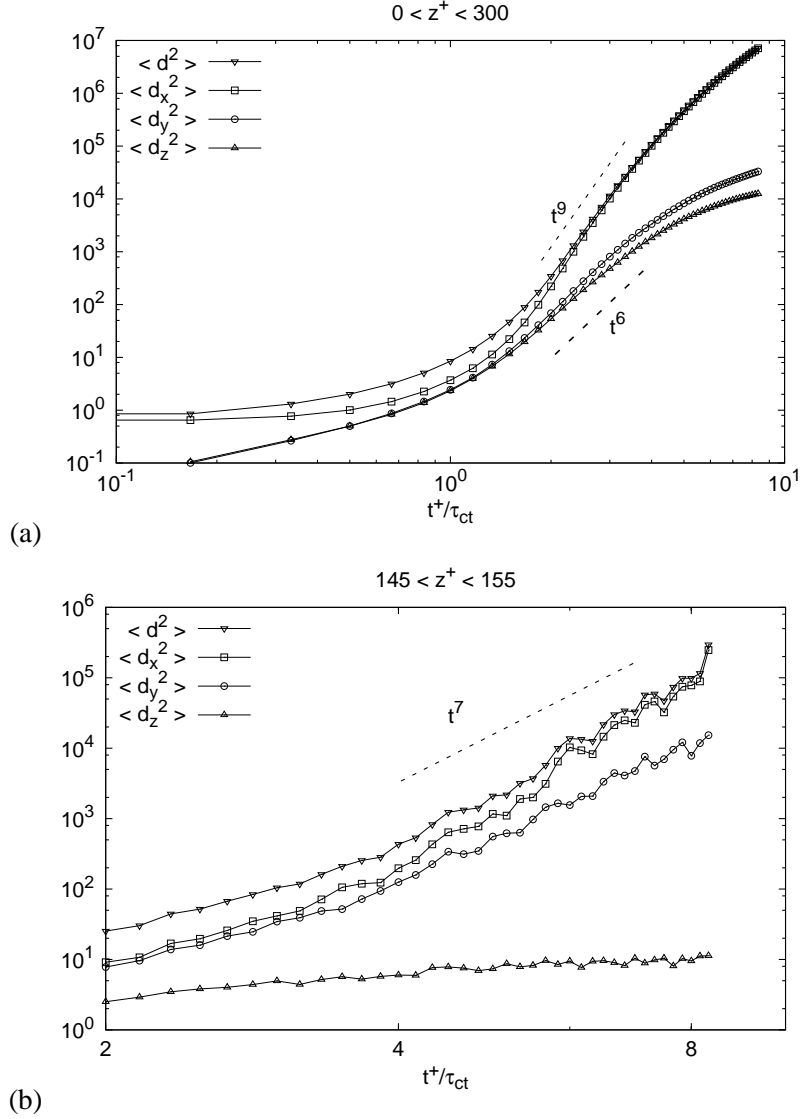


Figure 3.19: The mean square pair distance  $\langle d^2 \rangle$  compared with its three components:  $\langle d_x^2 \rangle$ ,  $\langle d_y^2 \rangle$  and  $\langle d_z^2 \rangle$ . At small times ( $t^+/\tau_{ct} < 1$ ),  $\langle d_x^2 \rangle \approx \langle d_y^2 \rangle \approx \langle d_z^2 \rangle$ . (a) At larger times ( $2 < t^+/\tau_{ct} < 3$ ), corresponding to the inertial sub-range,  $\langle d^2 \rangle \approx \langle d_x^2 \rangle \sim t^9$  and  $\langle d_z^2 \rangle \sim t^6$ . Statistics are calculated on the all pairs. Particles are released at  $z_0^+ = 150$  oriented along the streamwise direction. A similar behavior was found for other wall normal locations and initial orientations. (b) At larger times ( $t^+/\tau_{ct} > 4$ ),  $\langle d^2 \rangle \approx \langle d_x^2 \rangle \sim t^7$ . Statistics are calculated only on the pairs that remain confined in the center of the channel, in the slab  $145 < z^+ < 155$ . The fluctuating trends of the lines at the end of the graph is due to the small number of pairs still within the very thin slab at long times. Slopes are plotted just as trendlines (no data fit).

We can try to reduce the action of the shear calculating the mean square separation  $\langle d^2 \rangle$  of particles released at the center channel and only for pairs

that remain within a slab of flow symmetric to the centerline, so that they are exposed at smaller differences of streamwise velocity. It seems that the thinner the slab the slower the dispersion, as expected. We can also fit this trends with the exponential function  $f(t) = t^\alpha$  in order to get a more accurate estimate of the exponent  $\alpha$  in the inertial subrange.

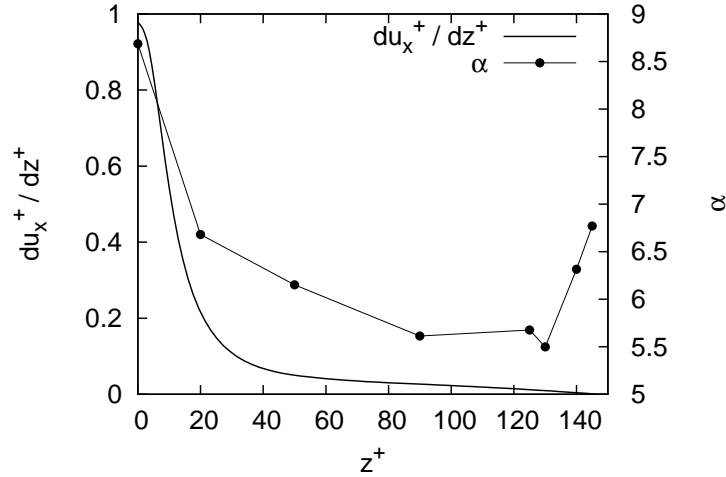


Figure 3.20: The exponent  $\alpha$  of the slope of  $\langle d^2 \rangle$  in the inertial subrange for particles initially placed at the centerline ( $z_0^+ = 150$ ) and for different slabs of statistics computation. The shear is superimposed for comparison purposes.

In Fig.3.20 values of  $\alpha$  are shown at the limit  $z^+$  coordinate for the corresponding slab. For instance, the value of  $\alpha$  at  $z^+ = 20$  is the exponent obtained calculating statistics between  $z^+ = 20$  and  $z^+ = 280$ . A similar trend for the shear and the exponent  $\alpha$  is found from  $z^+ = 0$  to  $z^+ = 90$  (monotonic decreasing). After that an increase of  $\alpha$  is appreciated, even if this latter is not so reliable, because of the fluctuating statistics values due to the small number of pairs still within the very thin slabs at long times.

This confined statistics allowed an evaluation of shear influence on pair dispersion. The exponent  $\alpha$  reaches the minimum value of 5.5, this latter being much less than 8.7 (obtained with statistics over the whole channel). However, the trend is still rather far from Richardson's one. It is interesting to note that at large times  $\langle d_x^2 \rangle$  becomes dominant even when statistics are confined very close to the centerline (Fig.3.19(b)). This means that pairs separate above all along streamwise direction even if the shear is almost null. This behavior is also found for all slabs of different thickness, namely when particles are both affected by turbulent fluctuations and by shear of different magnitude. This results suggest us that even if in the center channel some flow's statistics are

very similar to those in a homogeneous isotropic flow [22] and the shear is almost null, there must be some other causes for the different behavior in terms of pairs dispersion, probably because of the non-zero mean velocity (along streamwise direction) and because of the turbophoresis, that acts mainly in the nonhomogeneous wall normal direction. In Fig.3.19(b) the mean square pair dispersion and its three components are shown for statistics confined to the thinner slab ( $145 < z^+ < 155$ ).

As mentioned above, the *total exit time* provides a good measure of pair dispersion, in agreement with the trend obtained calculating  $\langle d(t)^2 \rangle$  (see Fig.3.10). This agreement is found because every exit time refers to the initial time ( $t = 0$ ), when particles of each pair were very close to each other and every pair was placed at the same wall normal coordinate. This is no longer true in the computation of the *exit time* (Fig.3.13), for which we calculate the average time taken for the pair separation to change from a threshold to the next one. This statistic does not refer to the initial separation and location of each pair and then it is affected by the instantaneous position of the particles. Hence the reasons of the non-monotonous trend of  $\langle T_p(d) \rangle$  are not completely understood. Looking for instance at Fig.3.13(a), we notice that when the graph reaches its first local minimum value, i.e. at  $d \cong 20$ , the effect of the shear is predominant and  $\langle d^2 \rangle \approx \langle d_x^2 \rangle$ , as clearly visible in Fig.3.19. This means that at the eighth threshold, namely at  $d_8 = \rho^8 d_0 \cong 19.6$ , particles of each pair are almost completely decorrelated and so an explanation for the local maximum at  $d \cong 150$  and the other local minimum at  $d \cong 500$  is not easy to find. A similar discussion can be provided for the *mean longitudinal exit velocity* (Fig.3.16).

A previous work by Celani *et al.* [7] reveals results very similar to our. They superimposed an average linear shear and a turbulent fluctuating field on a two-dimensional domain, in order to study the effects on the energy spectrum. They illustrate the physical mechanisms in terms of the motion of Lagrangian particles. Their results are shown in Fig.3.21(a) and 3.22(a). At small times, the Richardson prediction is recovered and the anisotropy induced by the shear is negligible. As the separation becomes larger compared to the characteristic length scale of the shear, the latter affects the trajectories and  $\langle d^2 \rangle \approx \langle d_x^2 \rangle \gg \langle d_y^2 \rangle$ , where the subscript  $y$  refers to the component orthogonal to the shear (that we name  $z$ ). In particular, in this range of scales,  $\langle d_x^2 \rangle \sim t^9$  and  $\langle d_y^2 \rangle \sim t^7$ . Similarly, we find  $\langle d^2 \rangle \approx \langle d_x^2 \rangle \sim t^9$  in the inertial subrange, even if for a smaller range of time (see slope in Fig. 3.21(c)). Wall normal component cannot reach the inertial subrange before being affected by the shear and it follows  $\langle d_z^2 \rangle \sim t^6$  at the end of the dissipation subrange. Fi-

nally, we do not observe any plateau around the slope  $\sim t^3$  in the dissipation subrange. In Fig.3.22(a) we plot the quantity  $S_2(r,0)$ , that Celani *et al.* say being proportional to "the time for two particles, initially coinciding, to reach a separation  $r$ ", exactly what we name *total exit time*. Thus we can compare  $S_2(r,0)$  with  $\langle T_\rho(d) \rangle$ , that is displayed in Fig.3.22(b). As mentioned above, this statistic shows the *uncontaminated* behavior of the particles at several pair distances. Indeed the plateau at  $2/9 \approx 0.22$  in the inertial subrange is well appreciated in the slope (Fig.3.22(c)).

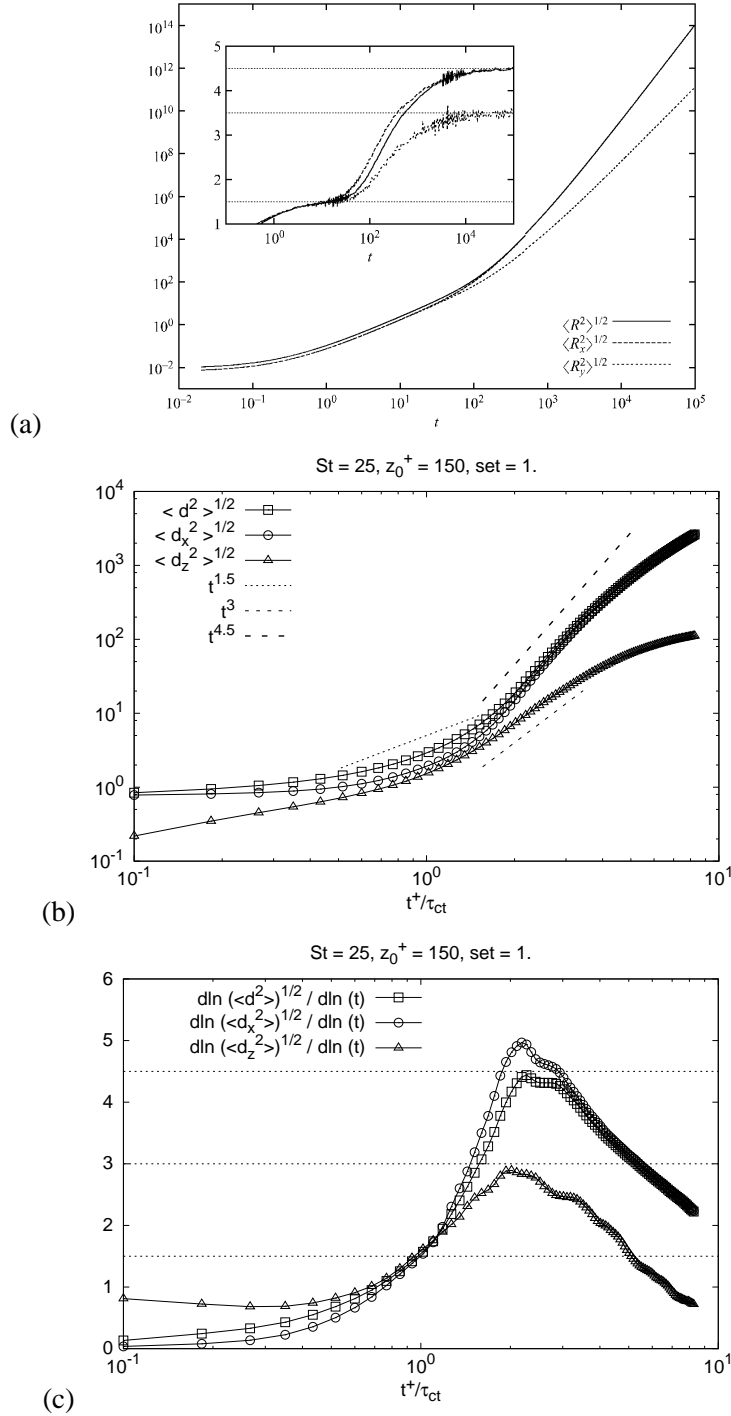


Figure 3.21: Comparison between present results and results of Celani *et al.* [7] (a) At small times, Celani *et al.* recover Richardson prediction, while the anisotropy induced by the shear is negligible. As the separation becomes larger compared to the characteristic length scale of the shear, the latter affects particles trajectories and  $\langle d^2 \rangle \approx \langle d_x^2 \rangle \gg \langle d_y^2 \rangle$ , where the subscript  $y$  refers to the component orthogonal to the shear (that we name  $z$ ). In this range of scales,  $\langle d_x^2 \rangle \sim t^9$  and  $\langle d_y^2 \rangle \sim t^7$ . (b) Similarly, we find  $\langle d^2 \rangle \approx \langle d_x^2 \rangle \sim t^9$  in the inertial subrange, even if for a smaller range of time. The wall normal component cannot reach the inertial subrange before being affected by the shear and it evolves as  $\langle d_z^2 \rangle \sim t^6$  at the end of the dissipation subrange. Slopes are plotted just as trendlines (no data fit). (c) No plateau is observed around the slope  $\sim t^3$  in the dissipation subrange.

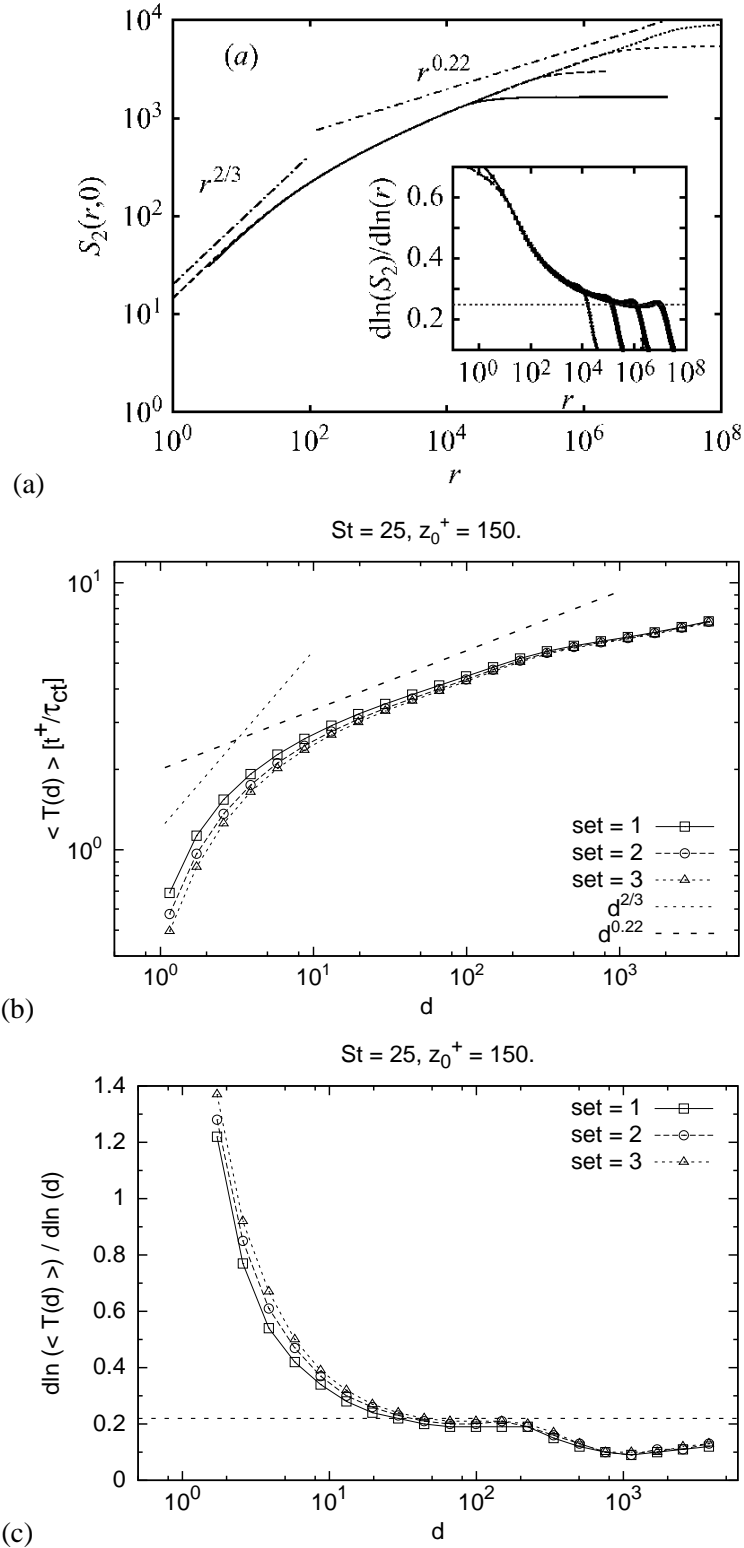


Figure 3.22: Comparison between present results and results of Celani *et al.* [7]. In Celani *et al.* the quantity  $S_2(r,0)$ , shown in panel (a), is proportional to the time for two particles, initially coinciding, to reach a separation  $r$ , which is exactly the *total meanexit time*, shown in panel (b). Slopes are plotted just as trendlines (no data fit). This statistic shows the *uncontaminated* behavior of the particles pairs at several inter-particle distances. The plateau of the slope at a value of  $2/9 \approx 0.22$  in the inertial subrange is well appreciated (c).



## Chapter 4

# Conclusions

In this work we analyzed the dispersion of micrometer size inertial particles by examining the behavior of particles pairs injected in a non-homogeneous and anisotropic turbulent shear flow. Pseudo-spectral Direct Numerical Simulation was carried out to calculate the flow field at friction Reynolds number  $Re_\tau = 150$  in a 4 cm - high channel. Lagrangian tracking was used to describe the motion of large swarms of particles with different inertia, precisely with size  $d_p \cong 45, 100$  and  $230 \mu m$ , corresponding to  $St = 5, 25$  and  $125$  respectively.

First, we showed time-dependent PDFs of single-particle distributions inside the flow domain. We noticed that the dispersion of the particles follows different laws for swarms injected at different wall normal locations. In particular, particles released at the center of the channel spread to the walls with a Gaussian behavior, while most of the particles injected near the walls remain very close to their initial wall normal coordinate. We fitted data of these two swarms and we created a simple parametric model to predict particles spreading from the injection planes to the rest of the channel. This model can be applied in a lot of real situations, such as for studies of smoke dispersion by a chimney or by a fire in the atmospheric boundary layer.

Then, we showed particle pair dispersion, through both fixed-time and fixed-scale statistics, the latter used to display an *uncontaminated* inertial subrange, i.e. not affected by the different separation rate of pairs that separate slowly and those that separate rapidly. We found a very strong deviation from Richardson's scaling  $\sim t^3$  in the inertial subrange in isotropic homogeneous turbulence. Indeed, pairs separate proportionally to  $t^\alpha$ , where  $\alpha$  varies from 4 up to 9 depending on their Stokes number, wall normal coordinate of injection and initial orientation. We justified this trends by the action of the shear, but we

found  $\alpha > 3$  even when statistics are confined around the nearly-homogeneous central region of the channel. So there must be other reasons for this deviation from Richardson's law, probably due to the non-zero mean velocity profile along streamwise direction or to the turbophoresis. We compared our results with results of Celani *et al.*[7]. They superimposed an average linear shear and a turbulent fluctuating field on a two-dimensional domain, in order to study the effects on the energy spectrum. They illustrate the physical mechanisms in terms of the motion of Lagrangian particles. We both found that at small times, the anisotropy induced by the shear is negligible, but as the separation becomes larger compared to the characteristic length scale of the shear, the latter affects the trajectories and  $\langle d^2 \rangle \approx \langle d_x^2 \rangle \gg \langle d_z^2 \rangle$ . In particular we both obtained  $\langle d_x^2 \rangle \sim t^9$  in the inertial subrange.

Finally, we propose some future developments. The reasons of the deviation of pair dispersion from Richardson's law have to be found. To this aim, tracer particles should be tracked, so that they sample the phenomenon of dispersion without any low-pass filter due to inertia, providing a more accurate action of the small-scales of turbulence on pair separation. After that, the parametric study in the  $(Re_\tau, St)$  space should be expanded, in order to get a more complete collection of results at several configurations of the system fluid turbulence-inertial particles. Finally, the filtering effects of the flow field on particle pair dispersion have to be studied, to get an estimate of the errors introduced by Large Eddy Simulations.

# Bibliography

- [1] R. J. Adrian, C. D. Meinhart, and C. D. Tomkins, *J. Fluid Mech.* **422**, 1–54 (2000).
- [2] L. Biferale, G. Boffetta, A. Celani, B. J. Devenish, A. Lanotte, F. Toschi, "Lagrangian statistics of particle pairs in homogeneous isotropic turbulence", *Phys. of Fluids* **17**: 115101 (2005).
- [3] G. Boffetta and I.M. Sokolov, "Statistics of two-particle dispersion in two-dimensional turbulence", *Phys. of Fluids Vol* **14**, 3224-3232 (2002).
- [4] J.W. Brooke, K. Kontomaris, T. J. Hanratty, and J. B. McLaughlin, *Phys. Fluids A* **4**, 825–834 (1992).
- [5] M. Campolo, M. V. Salvetti, and A. Soldati, *AIChE J.* **51**, 28-43 (2005).
- [6] M. Caporaloni, F. Tampieri, F. Trombetti, and O. Vittori, *J. Atmos. Sci. (USA)* **32**, 565–568 (1975).
- [7] A. Celani, M. Cencini, M. Vergassola, E. Villermaux, and D. Vincenzi, "Shear effects on passive scalar spectra", *J. Fluid Mech.* **523**, 99-108 (2005).
- [8] J.W. Cleaver and B. Yates, *Chem. Eng. Sci.* **30**, 983–992 (1975).
- [9] R. Clift, J.R. Grace, M.E. Weber, "Bubbles, Drops and Particles" Academic Press (1978).
- [10] J. K. Eaton and J. R. Fessler, *Int. J. Multiph. Flow* **20**, 169–209 (1994).
- [11] S. K. Friedlander and H. F. Johnstone, *Ind. Eng. Chem. Res.* **49**, 1151–1156 (1957).
- [12] J. C. R. Hunt, A.A. Wray, and P. Moin, Center of Turbulence Research Rep. CTR-S88, 193 (1998).

- [13] F. Hussain, *Phys. Fluids* **26**, 2816–2838 (1983).
- [14] I. Iliopoulos and T. J. Hanratty, “Turbulent dispersion in a non-homogeneous field”, *J. Fluid Mech.* **392**, 45–71 (1999).
- [15] J. Jeong, F. Hussain, W. Schoppa, and J. Kim, *J. Fluid Mech.* **332**, 185–214 (1997).
- [16] M. C. Jullien, J. Paret, and P. Tabelling, “Richardson Pair Dispersion in Two-Dimensional Turbulence”, *Phys. Review Letters* Vol **82**, 2872–2875 (1999).
- [17] C. Jung-II, Y. Kyongmin, and L. Changhoon, “Lagrangian statistics in turbulent channel flow”, *Phys. Fluids* **16**, 779–793 (2004).
- [18] D. Kaftori, G. Hetsroni, and S. Banerjee, *Phys. Fluids* **7**, 1107–1121 (1995).
- [19] K. M. Kajal, B. S. Mazumder, “Dispersion of fine settling particles from an elevated source in an oscillatory turbulent flow”, *Eur. J. of Mech. B/Fluids* **27**, 707–725 (2008).
- [20] J. Kim and F. Hussain, *Phys. Fluids A* **5**, 695–706 (1993).
- [21] S. J. Kline, W. C. Reynolds, F.A. Schraub, and P.W. Runstadler, *J. Fluid Mech.* **70**, 741–773 (1967).
- [22] C. Marchioli, M. Picciotto, and A. Soldati, “Particle dispersion and wall-dependent turbulent flow scales: implications for local equilibrium models”, *J. of Turbulence* **60**, (2006).
- [23] C. Marchioli and A. Soldati, *J. Fluid Mech.* **468**, 283–315 (2002).
- [24] M. R. Maxey and J. J. Riley, *Phys. Fluids* **26**, 883–889 (1983).
- [25] M. R. Maxey, *Phys. Fluids* **30**, 1915–1928 (1987).
- [26] J. B. McLaughlin, *Phys. Fluids* **1**, 1211–1224 (1989).
- [27] A. Perry and M. S. Chong, *Ann. Rev. Fluid Mech.* **9**, 125–148 (1987).
- [28] L. M. Portela, P. Cota, and R.V.A. Oliemans, *Powder Technol.* **125**, 149–157 (2002).
- [29] Salazar J.P.L.C. and Collins L.R., “Two-particle dispersion in isotropic turbulent flows”, *Annu. Rev. Fluid Mech.* **41**, 405–32 (2009).

- [30] F. Sbrizzai, R. Verzicco, M. Pidria and A. Soldati, *Int. J. Multiph. Flow* **30**, 1389–1417 (2004).
- [31] V. L. Schiller, A. Naumann, "Über die grundlegenden Berechnungen bei der Schwerkraftaufbereitung", *Z. Ver. Deut. Ing.* **77**, 318-320 (1935).
- [32] W. Schoppa and F. Hussain, in: *Self-sustaining Mechanisms of Wall Turbulence*, edited by R. Panton (Computational Mechanics Publications Vol. 15), (WIT Press, Shouthampton, 1997), 385–422.
- [33] A. Soldati, M. Casal, P. Andreussi, and S. Banerjee, "Lagrangian Simulation of Turbulent Particle Dispersion in Electrostatic Precipitators", *AIChE Journal* **43**, 1403-1413 (1997).
- [34] A. Soldati, "Particles turbulence interactions in boundary layers", *ZAMM - J. Applied Math. and Mech.* **85**, 683-699 (2005).
- [35] W.W. Willmarth and S. S. Lu, *J. Fluid Mech.* **55**, 65–92 (1972).
- [36] P. K. Yeung and S.B. Pope, "An algorithm for tracking fluid particles in numerical simulations of homogeneous turbulence" *J. Comput. Phys.* **79**, 373-416 (1988).
- [37] J. Zhou, R. J. Adrian, S. Balachandar, and T. M. Kendall, *J. Fluid Mech.* **387**, 353–396 (1999).